Improved Models of Joined Sheet Metal Beam Structures for Vehicle Safety Studies

Undergraduate Honors Thesis

Presented in Partial Fulfillment of the Requirements for Graduation with Distinction in the Department of Mechanical Engineering at The Ohio State University

By

Kelley Elizabeth Dugan

Undergraduate Program in Mechanical Engineering

The Ohio State University

2017

Advisors: Scott Noll and Rajendra Singh

Copyrighted by

Kelley Elizabeth Dugan

2017

Abstract

This research was motivated by the practical need of the automotive industry to enhance simulation technology for use in crash sensor calibration prior to the construction of a physical prototype. This study aimed to aid in developing connection models and damping parameters for use in full-scale vehicle crash models. In particular, prior literature has suggested the need to extend the frequency range up to at least 400 Hz for simulation technology. The purpose of this research was to create computational (finite element) models of sheet metal beam structures that are joined using spot welds and structural adhesives. Benchmark laboratory (modal type) experiments were conducted to assist with validation of the finite element model with emphasis on the connection properties. Dynamic accelerations and forces (under controlled impulsive loading) were measured to compare to the model predictions in both the frequency and time domains. Parameters of the model that were examined include mesh size, part thickness, contact, and interfacial damping models. Frequency domain analysis results show that the double hat section specimens used in this study, which were joined with structural adhesives and spot welds, can be idealized as having rigid connections with light material damping. Conversely, the double hat section specimen joined via spot welds alone exhibits significantly higher damping due to dissipation mechanisms within the interface. Furthermore, differences in modeling techniques showed that results from the frequency domain could not be directly translated to the time domain formulation.

Acknowledgements

First of all, I would like to thank my advisors, Dr. Rajendra Singh and Dr. Scott Noll, for bringing me on to this undergraduate research project. I would also like to thank Dr. Scott Noll for his continuous guidance and feedback during our weekly meetings. From providing concept video tutorials to lending out his text on mechanical vibrations for long periods of time and from steep learning curves to light bulbs, this research would not have been the same without his support. I appreciate the Acoustics and Dynamics Laboratory for letting me use test equipment and samples, crucial to obtaining experimental data and validating the finite element models.

I would like to thank the Simulation Innovation and Modeling Center for all the support I have received through funding and access to experts. I cannot imagine my Ohio State experience without it. Specifically, I am grateful to Dr. Shawn Midlam-Mohler for referring me to Dr. Scott Noll. In addition, I would like to thank Emily Nutwell for her finite element modeling tips, inspiration, and letting me borrow her Abaqus binder for the better part of my senior year.

Last but certainly not least, I would like to thank my four roommates and my best friend. Their emotional support, encouragement, and understanding kept me optimistic throughout the rough patches of the project.

Table of Contents

List of Figures

List of Tables

Chapter 1: Introduction

1A. Significance of Research

Medically consulted motor-vehicle injuries are very common, with an estimated 4.4 million occurring in 2015. In addition, in 2015 motor-vehicle deaths were up 8% from the previous year and totaled 38,300. This equates to 1.22 deaths per 100 million vehicle miles driven, which is up 5% from 2014 (NSC, 2015).

One ubiquitous automotive industry method for improving occupant safety has been the use of airbags or supplemental inflatable restraints (SIR), shown in Figure1A.1. In the event of a crash, the car's electronic control unit (ECU) uses signal inputs from remote sensors, shown in Figure 1A.2, to decide whether or not to deploy SIR. When a decision to deploy SIR is made, a signal is sent from the ECU to the inflator airbag module. If a vehicle occupant is too close to or in contact with the airbag when deployment begins they can be injured because airbags can inflate in less than 50 msec (NHTSA, 2017).

Figure 1A.1: Rendering of supplemental inflatable restraint system inside of vehicle (Air bags and air curtains, n.d.).

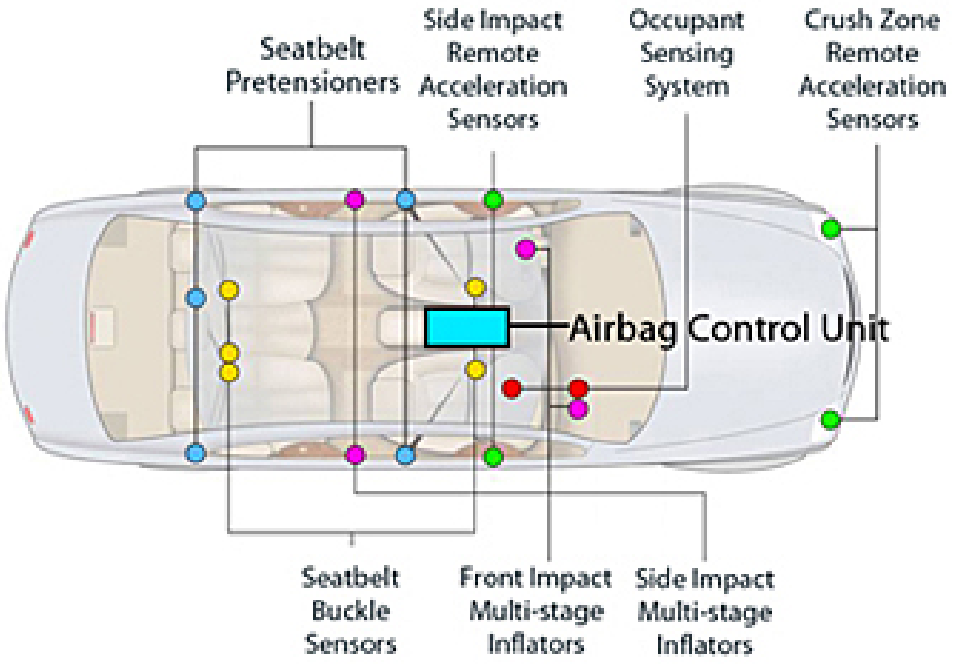

Figure 1A.2: Electronic Control Unit (ECU) remote sensors (Airbag control unit, n.d.).

After the initial impact the decision of whether or not to deploy SIR typically occurs within 8 to 40 msec (Huffman, 2011). This short timeframe for decision-making is imposed by the physical constraints of lag between when the signal is sent to deploy SIR and its deployment and the motion of vehicle occupants.

Crash sensor algorithm development and calibration relies mainly on performing physical crash testing for an array of crash modes, which occurs late in the vehicle development process. Another potential method of obtaining the crash signals necessary for crash sensor development is the use of computer-aided engineering (CAE) such as finite element analysis (FEA). Previous research in the development of CAE simulated crash pulses for airbag sensor algorithms and airbag sensor calibrations in frontal impacts identified two main components of a crash signal. The "crash base pulse" or low frequency response captures rigid body motion. The "shock or noise" is the high frequency response

which is the oscillatory or vibratory motion (Chou, 2001). This research showed that crash pulses are dominated by low frequencies; those less than 50 Hz. Contemporary CAE capabilities accurate up to 150 Hz account for the good overall correlation seen between physical testing and model results. However, poor correlation for the first 15 msec of data, which is a significant amount of time in the SIR deployment decision period, was identified. As well as, a need to obtain accurate frequency data up to 400 Hz in order for simulated crash pulses to be used.

One illustrative example of the cost and time savings afforded by the use of computer simulation in industry is Jaguar Land Rover (Gibbs, 2015). Through the use of simulation, they have been able to reduce, from 30 to 50 to 10 to 15, the number of crash-test prototypes necessary for crash-testing a new vehicle model. Since each prototype costs approximately $777,000, there are clearly significant cost savings.

Acceleration based crash algorithms, in comparison to velocity based, allows for earlier airbag deployment decision for complex crash modes (Stutzler, 2003). The ability to detect a crash event early in the pulse leads to early airbag deployment times and ultimately improved safety performance of the vehicle restraint system. So within the automotive industry, there is a desire to have a robust method of predicting acceleration based crash sensor signals during both high and low-speed crash events at the design of a vehicle. This information could then be used to interface with automotive suppliers during the development of the vehicle instead of having to wait until a physical vehicle model can be crash tested. Crash algorithms have to be able to differentiate between various transient impulses in order to provide the correct response actions. For example, they must

differentiate between a vehicle encounter with potholes, street curbs, door slams, low speed crash, or high speed crash.

1B. Problem Formulation

This research focuses on experiments and models of double hat section steel sheet metal beam structures of passenger vehicles. This allows the model size and complexity to be reduced to one that can be iterated on relatively fast as compared to a full vehicle model. A B-pillar is a vertical structural support located at the rear of driver and passenger door as shown in Figure 1.B1. One situation in which crash sensors located on the B-pillar would be relevant is a side impact test as shown in Figure 1.B2.

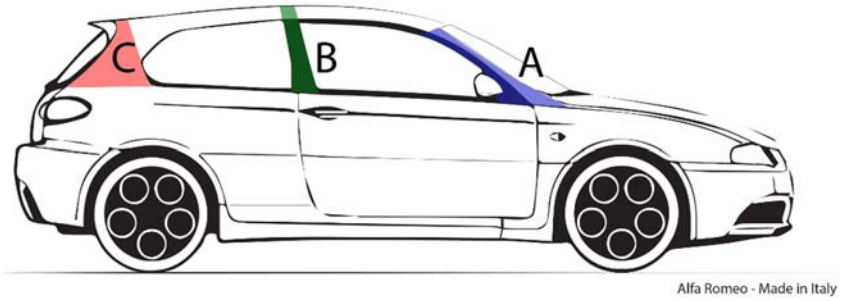

Figure 1B.1: Location of B-pillar in automobile (Pava, 2015).

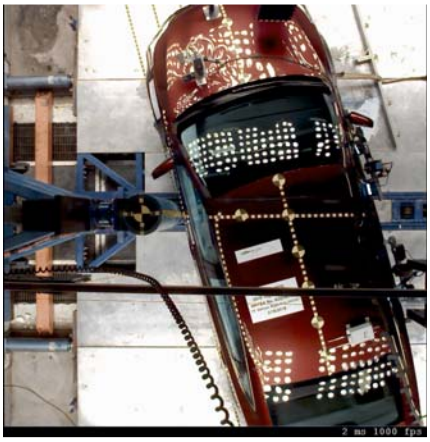

Figure 1B.2: Side impact into rigid pole crash test (Camera No. 10 – Overhead Wide View of Impact.avi, n.d.).

Steel is commonly used in the automotive industry given its ability to achieve structural performance characteristics of high strength and stiffness, while maintaining relatively lightweight characteristics (Ghassemeih, 2001). The sheet metal structural members used in automotive applications are often joined using spot welds, bolts, and structural adhesives. A picture of a vehicle B-pillar is shown in Figure 1.B3. Given that it is a hollow cross-section with spot welds along its flanges, a double hat section, as shown in Figure 1B.4, which shares those key characteristics, was used as a simplified model of the B-pillar.

Figure 1B.3: Vehicle B-pillar hollow section (BMW 7-series, n.d.).

Figure 1B.4: Double hat section test piece.

The purpose of this research was to create computational models, which capture the high frequency response, of sheet metal beam structures that were joined using spot welds and structural adhesives. This was broken down into three specific objectives as follows:

1. Construct and conduct benchmark experiments to assist in the development and validation of finite element models in both the frequency and time domains;
2. Construct finite element models of double hat section sheet metal beam structures and to conduct both mesh and element sensitivity analyses on these FEM;
3. Investigate various spot weld and interface connection modeling schemes, with focus on the evaluation of different damping model types and estimation of both part and connection damping properties.

In addition, the scope of this research is limited to the small-amplitude response of the structure that is away from the crush zone and thus no plastic deformation of the part occurs. Given that crash algorithms need to differentiate between transient impulses the research is analyzing transient phenomenon by applying an impulse excitation to the sheet metal beam structure. Both the benchmark experiments and finite element models are assuming a linear analysis at an operating point is sufficient.

1C. Overview of Thesis

This thesis consists of five chapters. Chapter 2 explains the experimental setup and data collection procedures. It also includes a brief discussion of the results obtained from physical measurements. Chapter 3 describes the initial creation of the finite element models, while Chapter 4 presents the results of various models and how they were

iteratively determined. Chapter 5 summarizes the findings of this research and Chapter 6 suggests a path for future work.

Chapter 2: Benchmark Experiments

2A. Experimental Setup

The benchmark experiments allowed for the measurement of the transfer function of the double hat section parts. A laptop with LMS Test.Lab software, a SCADAS data acquisition system, and an impulse hammer and accelerometer were used to measure the excitation and response of the double hat section test structures (LMS Test.Lab, 2015). The double hat section was supported by foam pads as shown in Figure 2A.1, which is a side view schematic of the double hat section, to approximate free-free boundary conditions.

Figure 2A.1: Side view schematic of double hat section showing approximation of free-free boundary conditions using foam pads (green rectangles).

Excitations were applied to six locations using an impulse hammer with a sensitivity of 2.52 mV/N shown in Figure 2A.2. These six excitation points were labeled from 1 to 6, which number 1 being closest to the edge of the part. Figure 2A.3 is a schematic outlining the exact location of the 6 points. An accelerometer with a nominal sensitivity of 10 mV/g was utilized to record the response of the part to the excitation and was located at position 1. Therefore, position 1 was the only driving point and all other positions were

cross points. The two locations this research focused on were position 1 and position 6. The term driving point will be used interchangeably with excitations applied at position 1, while cross point will be used interchangeably with excitations applied at position 6.

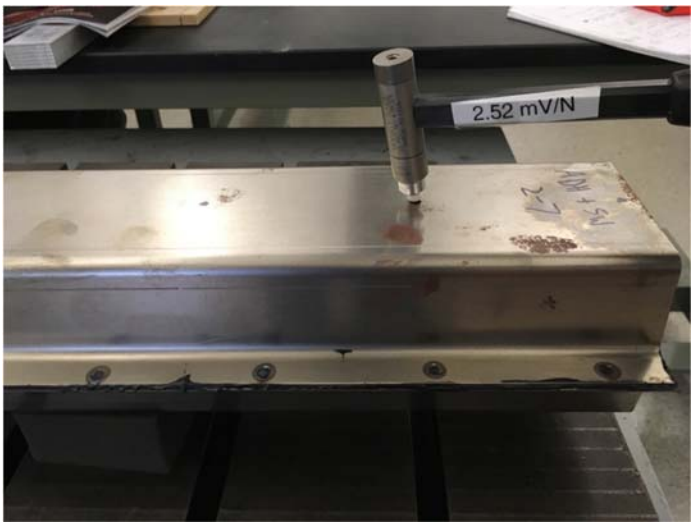

Figure 2A.2: Impulse hammer applied to position 1, which is the only driving point.

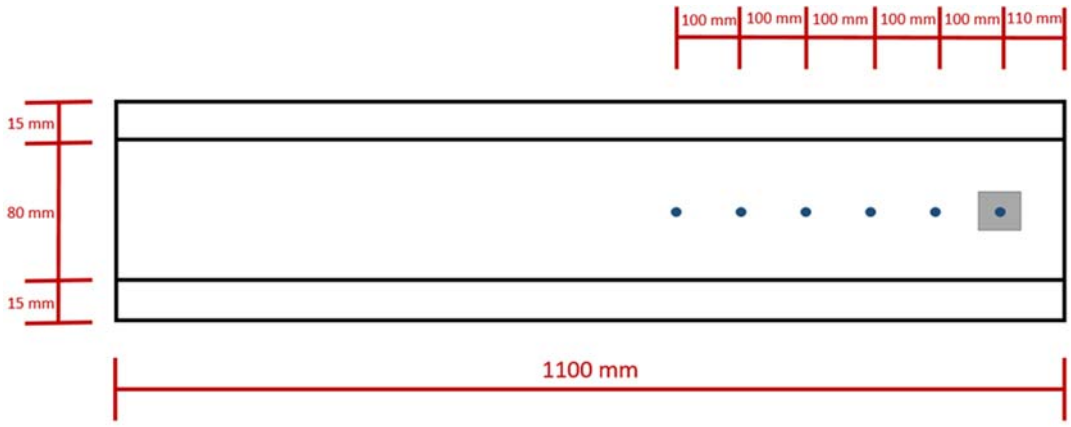

Figure 2A.3 Top view schematic of double hat section showing the excitation locations and accelerometer location. Key: (circle) excitation location (square) accelerometer location.

Three different double hat section parts were used for experimental data collection. Two of the double hat sections were joined using a combination of spot welds and structural adhesives. Having two parts with the same connection type allowed for the manufacturing

variability between parts to quantified. The third double hat section was joined using only spot welds. Table 2A.1, below, summarizes the double hat sections used for the benchmark experiments.

Table 2A.1: Double hat sections of Figure 2A.3 used for physical experiment data collection.

Part #	Spot Welds	Structural Adhesive	# of Connection Welds	Spot Weld Pitch (mm)	Spot Weld Radius (mm)
1	Yes	Yes	32	72.4	5
2	Yes	Yes			
3	Yes	No			

2B. Experimental Data

Figure 2B.1 is a plot of the magnitude frequency response function, for each of the parts, at position 1. Note that accelerance, acceleration per unit force, is plotted on a log scale (y-axis) against frequency on a linear scale (x-axis). The majority of the vibration modes are located within the 250 Hz to 500 Hz range. This is the high frequency or vibratory response that the finite element models aimed to capture. However, there are lower frequency modes that appear. These rigid body modes are all located below 10 Hz which is a factor of 25-30x smaller than the first flexural vibration mode and are the result of the foam pads not being able to provide ideal free-free boundary conditions.

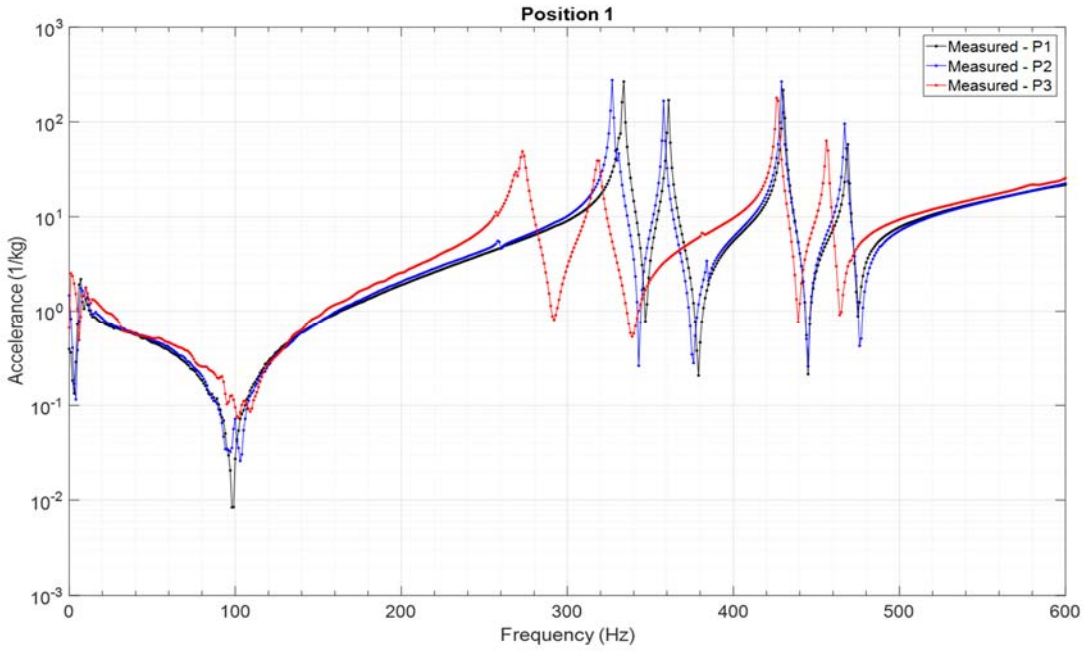

Figure 2B.1: Driving point accelerance for each test piece. Key: (—●—) measured data from Part 1; (—●—) measured data from Part 2; (—●—) measured data from Part 3.

Figure 2B.1 also shows that there are differences in the both the damping mechanisms and system stiffness between parts that are joined using a combination of structural adhesives and spot welds versus those joined using only spot welds. The difference in system stiffness is evident by part 3 having two peaks that are shifted to the left in comparison to parts 1 and 2, while the difference in the damping magnitude is evident, in part, by the lower accelerance amplitudes for the shifted peaks of part 3.

The part-to-part manufacturing variability was quantified by comparing the natural frequencies and peak amplitude accelerances of parts 1 and 2 at both position 1 and position 6. This manufacturing variability was quantified by a percent difference and later used to validate the finite element models. Table 2B.1 shows that at position 1 the percent difference in the location of the peaks, or their frequency, is limited to 2.12%, while their percent difference in the magnitude of the peaks accelerance is 50%. Table

2B.2 shows that at positon 6 the percent difference in the location of the peaks is limited to 2.12%, while their percent difference in the magnitude of the peaks is limited to 96%. The results from Table 2B.1 were used when evaluating the driving point and the results form Table 2B.2 were used when evaluating the cross point.

Table 2B.1: Part-to-part variability in driving point accelerance.

Position 1							
Natural Frequency (Hz)				**Magnitude of Peaks - Accelerance (1/kg)**			
Part 1	**Part 2**	**Difference (Hz)**	**Percent Difference (%)**	**Part 1**	**Part 2**	**Difference (1/kg)**	**Percent Difference (%)**
334	327	7.00	2.12	267.03	276.96	9.93	3.65
361	358	3.00	0.83	169.73	166.75	2.99	1.78
430	429	1.00	0.23	217.19	267.37	50.18	20.7
469	467	2.00	0.43	58.11	95.80	37.69	50.0

Table 2B.2: Part-to-part variability in cross point accelerance.

Position 6							
Natural Frequency (Hz)				**Magnitude of Peaks - Accelerance (1/kg)**			
Part 1	**Part 2**	**Difference (Hz)**	**Percent Difference (%)**	**Part 1**	**Part 2**	**Difference (Hz)**	**Percent Difference (%)**
334	327	4.00	2.12	38.84	109.87	63.77	95.53
331	330	4.00	0.30	46.1	48.57	9.73	5.21
361	358	3.00	0.83	177.54	190.51	12.97	7.05
430	429	1.00	0.23	213.24	260.86	47.62	20.09
`469	467	2.00	0.43	47.25	68.33	21.08	36.47

Chapter 3: Finite Element Model of the Double Hat Sections

The first step in creating the finite element model was replicating the geometry of the double hat section parts. Figure 3.1 shows the cross-section dimensions. These were the inputs used in Abaqus when creating an extruded part of a single hat section that was 1100 mm long. The elements were assigned a shell section. The section integration was

during analysis, with a thickness of 1.4 mm, using the Simpson thickness integration rule, and 5 thickness integration points. Two single hat section parts, the top and bottom sections, were used to make the Abaqus assembly (Abaqus CAE, 2014). The parts were separated by 1.4 mm to account for the section thickness. The final geometry model, shown in Figure 3.2, emulates the physical characteristics of the physical part, shown in Figure 1B.4.

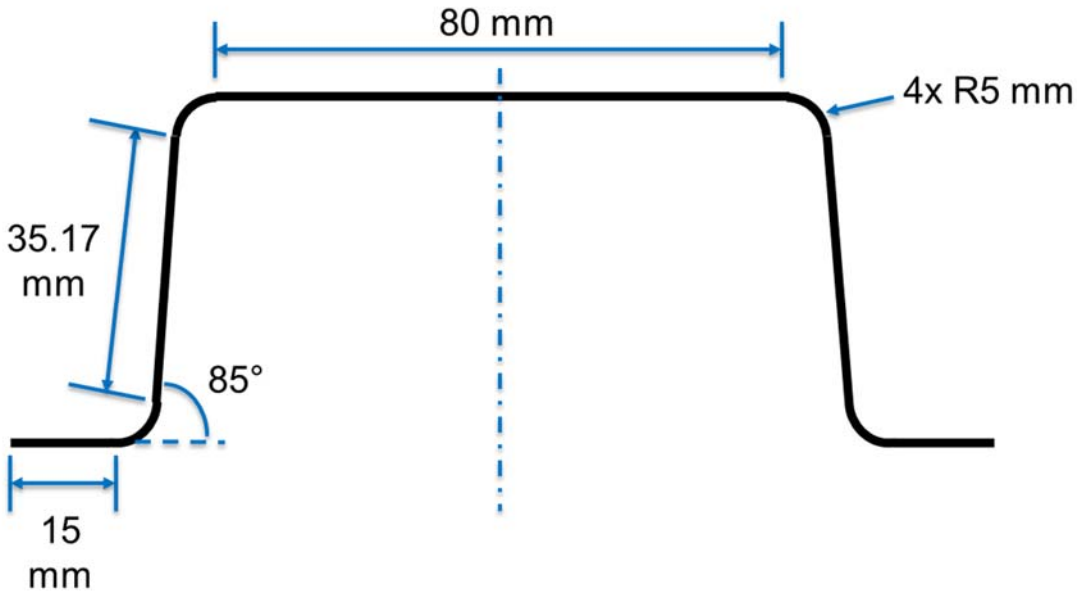

Figure 3.1: Schematic of double hat cross-section showing dimensions used to create model geometry.

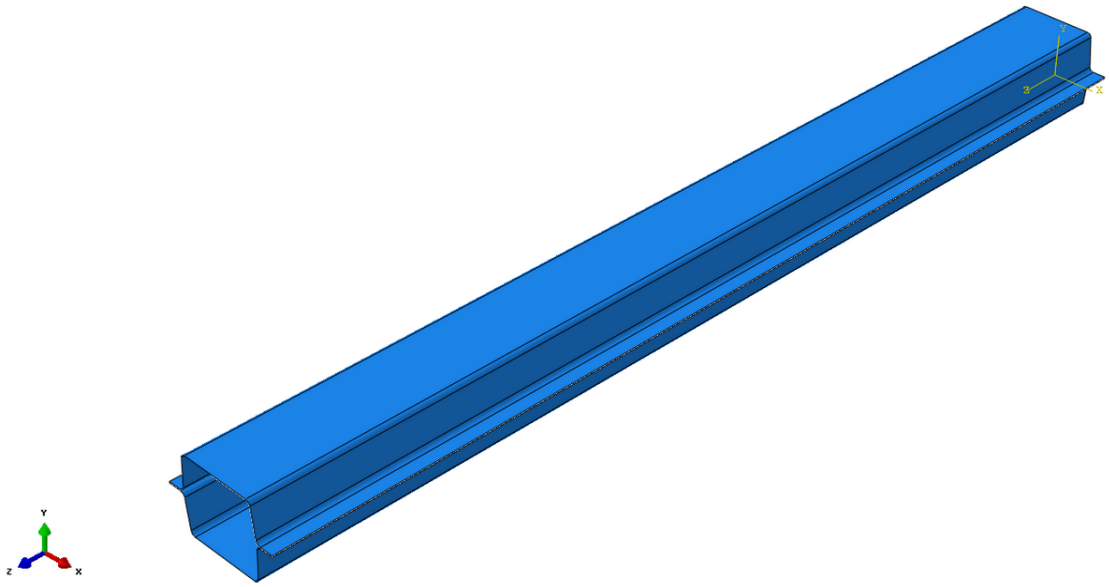

Figure 3.2: Abaqus model double hat section geometry.

Various thicknesses were analyzed to see if thickness had different effects at different frequencies. The results, shown in Figure 3.3 showed the same trend or no effect for the first 16 natural frequencies so the nominal thickness of 1.4 mm was used.

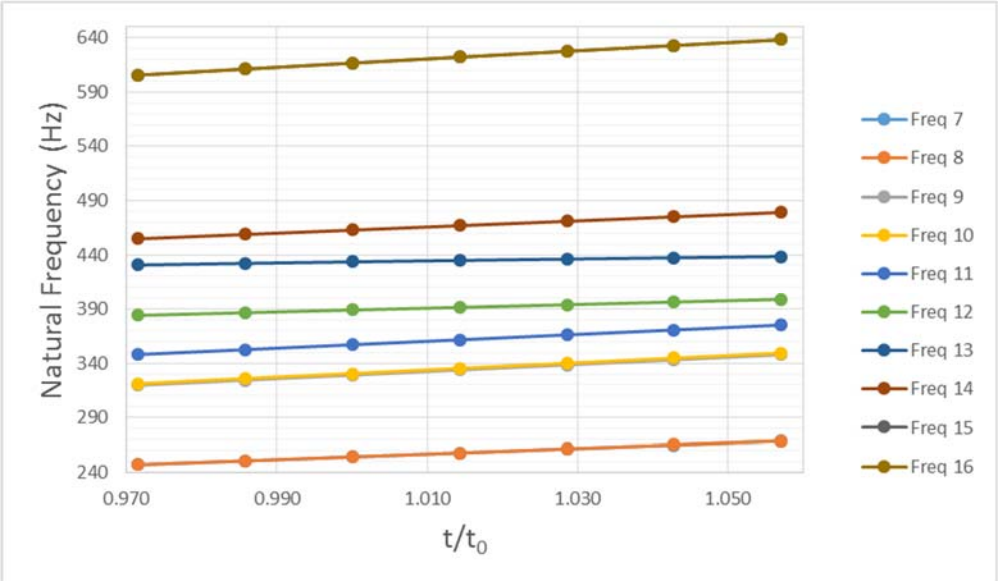

Figure 3.3: Normalized thickness parameter study of effect on natural frequency.

3A. Mesh Convergence with Tie Constraints

A mesh convergence study was performed to quantify the potential numerical error, with regard to element size and distribution, on the natural frequency up to 512 Hz. Natural frequency was the target of the convergence study and part thickness was set to 1.4 mm. Note that SI (mm) was the unit convention used in Abaqus throughout the entire thesis. The steel material property definitions used in the convergence study are summarized in Table 4A.1.

Table 4A.1: Material properties used for mesh convergence study

Material:	**Steel**
Density (tonne/mm^3)	7.85E-09
Young's Modulus (MPa):	200000
Poisson's Ratio	0.32

A tie constraint was used to hold the two hat-sections together. In which the master surface was the bottom side of the flanges from the top hat-section and the slave surface was the top side of the flanges from the bottom hat-section. Frequency steps were run using the Lanczos eigensolver.

Initially, the global element size was adjusted from 5 mm to 80 mm, doubling the approximate global size each time the frequency step was run for a total of 5 analyses. Global mesh refinement indicates element size along the longitudinal (z-direction) and along the cross-section (x-direction) are the same, as shown in Figure 3A.1

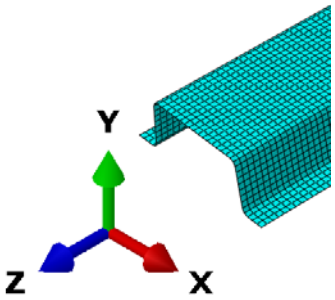

Figure 3A.1: Abaqus model orientation.

The frequency step requested the first 10 eigenvalues and standard linear quadrilateral quad-dominated (S4R) elements were used. The first 6 eigenvalues were zero because they represent rigid body motion for each degree-of-freedom (DOF). For convergence based on enforcing a percent change of 1% or less the model has converged for approximate global element sizes of 5 m and 10 mm using the data from the first four, nonzero, natural frequencies. Table 2B.3 provides visualization of the various mesh sizes evaluated.

Table 2B.3: Global mesh refinement results.

Total # of elements	19360	6160	1980	784	252
Approximate Global Size (mm)	5	10	20	40	80
f_7 (Hz)	253	254	260	286	363
f_8 (Hz)	253	255	260	286	364
f_9 (Hz)	328	330	338	375	429
f_{10} (Hz)	329	331	339	376	439
Percent Change =absolute($100*(f_2-f_1)/f_1$)					
f_7 (Hz)	0.56	2.24	9.06	21.09	-
f_8 (Hz)	0.53	2.22	9.02	21.29	-
f_9 (Hz)	0.59	2.50	9.82	12.56	-
f_{10} (Hz)	0.59	2.48	9.73	14.46	-

The global mesh was then kept constant at a size of 20 mm, while the number of elements along the length of the structure were adjusted. The frequency values did not change significantly because the global mesh size of 20 mm along the structures cross-section was too coarse. It was determined that the model was more sensitive along its cross-section, which is the width of the specimen, than along its length.

Then global mesh was then kept constant, while the number of elements along the cross-section of the structure were adjusted. This was done for a global mesh size of 20 mm, 40 mm, and 80 mm. The same results were obtained when explicit linear quadrilateral quad-dominated elements were used. Here convergence has been defined as a percent change of 0.3% or less because this will result in less than 2 Hz error for frequencies of 600 Hz. The results of first ten, nonzero, natural frequencies showed that the number of elements in the x-direction are more critical than the number of elements in the z-direction, because for each global element size the model has converged once the x-direction size is less than or equal to 2.5 mm. Figure 3A.2 provides visualization of this convergence for a global mesh size of 20 mm.

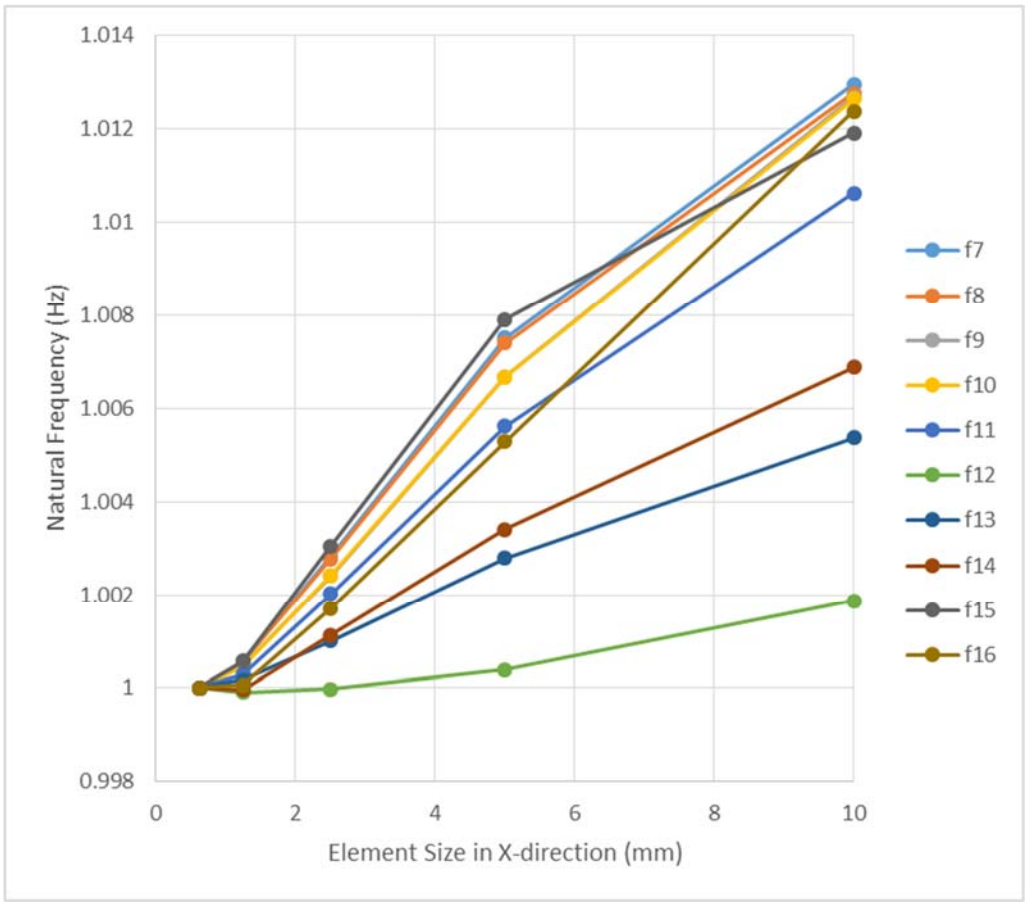

Figure 3A.2: Natural frequency convergence for global mesh size of 20 mm.

A new point of concern was brought up because of the fact that the natural frequencies converged to different values for different global mesh sizes. The accuracy of this model was evaluated by switching to the use of standard quadratic quadrilateral quad-dominated (S8R) elements. Again the global mesh was then kept constant, while the number of elements along the cross-section of the structure were adjusted. This was done for a global mesh size of 20 mm, 40 mm, and 80 mm. The results for the first ten, nonzero, natural frequencies provides confidence in the accuracy of the model because the natural frequencies converge to the same values for various global element size configurations.

Indeed, this was expected as quadratic elements are known to have better accuracy than linear elements.

Since coarser meshes require less computation time and the natural frequencies had already converged for all the configurations, the next step was to determine the least number of elements for which simulation results are still converged. Again, the global mesh was kept constant, while the number of elements along the length of the structure were adjusted.

To maintain a constant element size along the cross-section it was determined that the maximum element size in the x-direction is 5 mm. So the global mesh size used was 5 mm. The z-direction element size was evaluated at 20, 40, 80, and 160 mm. Here convergence was defined as a percent change of 0.3% or less. The results are summarized in Table 2B.4. The results for the first ten, nonzero, natural frequencies show that with using the maximum x-direction element size, the minimum z-direction size required for convergence is 80 mm. More detailed results and process from the mesh convergence study can be found in Appendix A.

Table 2B.4: Z-direction mesh refinement results.

Total # of Elements	4840	2464	1232	616
Approximate Global Size (mm)	20	40	80	160
X-dir Size	5	5	5	5
f_7 (Hz)	251	251	251	251
f_8 (Hz)	251	251	251	251
f_9 (Hz)	326	326	326	326
f_{10} (Hz)	327	327	327	327
f_{11} (Hz)	352	353	353	352
f_{12} (Hz)	383	383	383	382
f_{13} (Hz)	425	425	425	425
f_{14} (Hz)	456	456	456	459
f_{15} (Hz)	469	469	469	468
f_{16} (Hz)	607	607	608	621
Percent Change =absolute($100*(f_2-f_1)/f_1$)				
f_7 (Hz)	0.01	0.00	0.00	-
f_8 (Hz)	0.01	0.00	0.05	-
f_9 (Hz)	0.01	0.01	0.02	-
f_{10} (Hz)	0.01	0.04	0.02	-
f_{11} (Hz)	0.01	0.01	0.13	-
f_{12} (Hz)	0.01	0.02	0.05	-
f_{13} (Hz)	0.00	0.00	0.01	-
f_{14} (Hz)	0.01	0.03	0.62	-
f_{15} (Hz)	0.01	0.00	0.06	-
f_{16} (Hz)	0.01	0.08	2.11	-

3B. Final Mesh

To have nodes defined at the locations used in the physical experiment, partitions were created at the locations of positions 1 through 6. Partitions were created at 110, 210, 310, 410 510, and 610 mm from the left edge. The final mesh had an approximate global

element size of 40 mm, a cross-section element size of 5 mm, and 2112 quadratic quadrilateral elements of type S8R. Figure 3B.1 shows the transition from an unmeshed model with partitions to the meshed model.

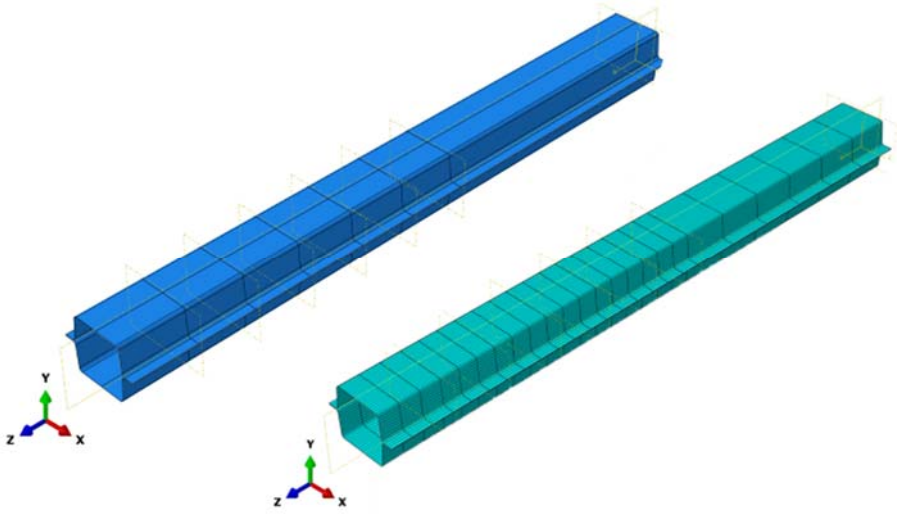

Figure 3B.1 Abaqus model transition from partition creation to mesh.

This final mesh in combination with provided material properties for the three physical parts created the baseline model that were adjusted depending on connection type and damping. Table 4B.1 summarizes these material properties.

Table 3B.1: Baseline material properties used in finite element model.

Material:	**Steel**
Density (tonne/mm^3)	7.80E-09
Mechanical Properties	
Elasticity:	Elastic
Type:	Isotropic
Young's Modulus (MPa):	207000
Poisson's Ratio	0.29

Chapter 4: Finite Element Model Iteration

4A. Abaqus Solution Methodologies

Three different solution steps were used in Abaqus depending on the desired output. In the frequency domain, there were two different steps: a frequency step and steady-state dynamics, direct solution step (Abaqus CAE, 2014). The frequency step used the Lanczos eigensolver, S8R elements, and requested the first 16 eigenvalues. The steady-state dynamics, direct solution step computed the complex response on a linear scale using S8R elements. The lower frequency was 1 Hz, the upper frequency was 512 Hz, and 512 points were requested with a bias of 1. The bias of 1 equally spaces the data points.

Within the time domain a static, general step was used in order to determine the stiffness of the hat section. The static general step used automatic incrementation with an initial and maximum increment size of 1 second and minimum incrementation size of 1.00E-05 seconds. The equation solver method was direct, S8R elements were used, and the full Newton solution technique was used. All other solution steps consisted of a double hat section with free-free boundary conditions, but the static general step consisted of a single hat section with ENCASTRE boundary conditions applied to the bottom side of the flanges. This boundary condition fixes the location of the part by setting all degrees of freedom of the flanges' nodes equal to zero.

4B. Frequency Domain – Spot Weld and Structural Adhesive Model

The first model created for frequency domain analysis of double hat sections that are joined using a combination of spot welds and structural adhesives did not include damping (Model D0). Within the Abaqus model, two single hat sections were joined along their flanges using a tie constraint, which rigidly connects every node along the flanges.

The tie constraint adequately captured the stiffness present in the physical parts 1 and 2 because the peak locations, which are the natural frequencies, aligned. However, Figure 4B.1 shows that there was physical light damping not captured by the model.

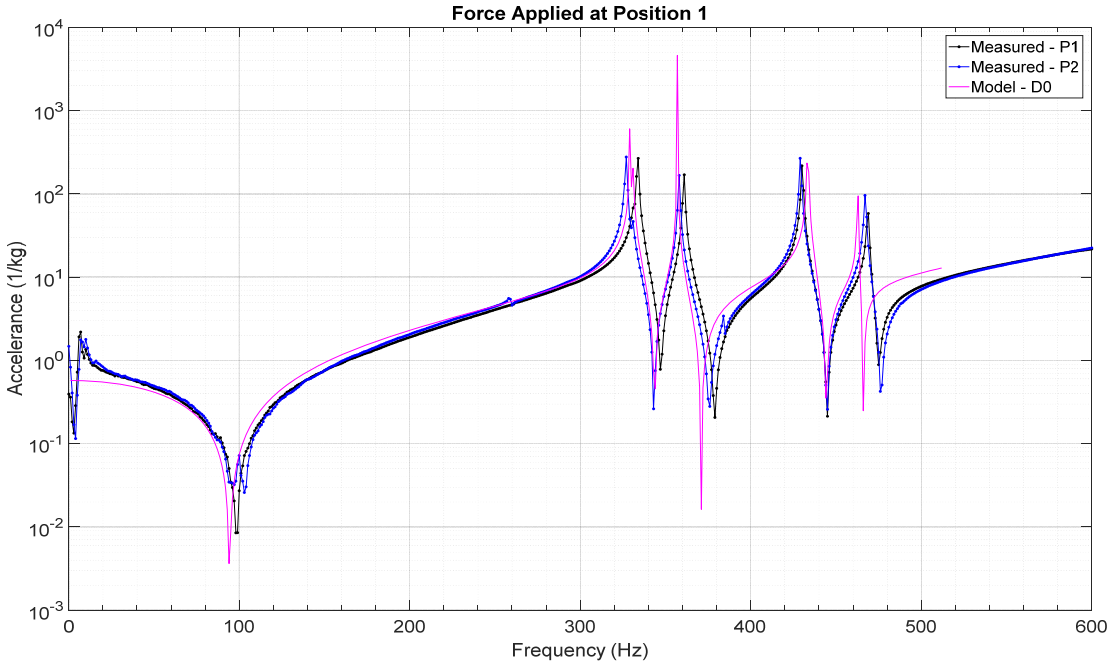

Figure 4B.1: Driving point accelerance for test pieces joined using both spot welds and structural adhesives and tie constraint model (Model D0).

The second model created, model D1, used a tie constraint along the flanges of the single hat section. In addition, a material structural damping factor was defined in the steel properties section of the model. Figure 4B.2 shows that this model was validated once a structural damping factor of 0.00128 was used. This value was found through iteration of structural damping factors, using peak magnitude as the updating parameter.

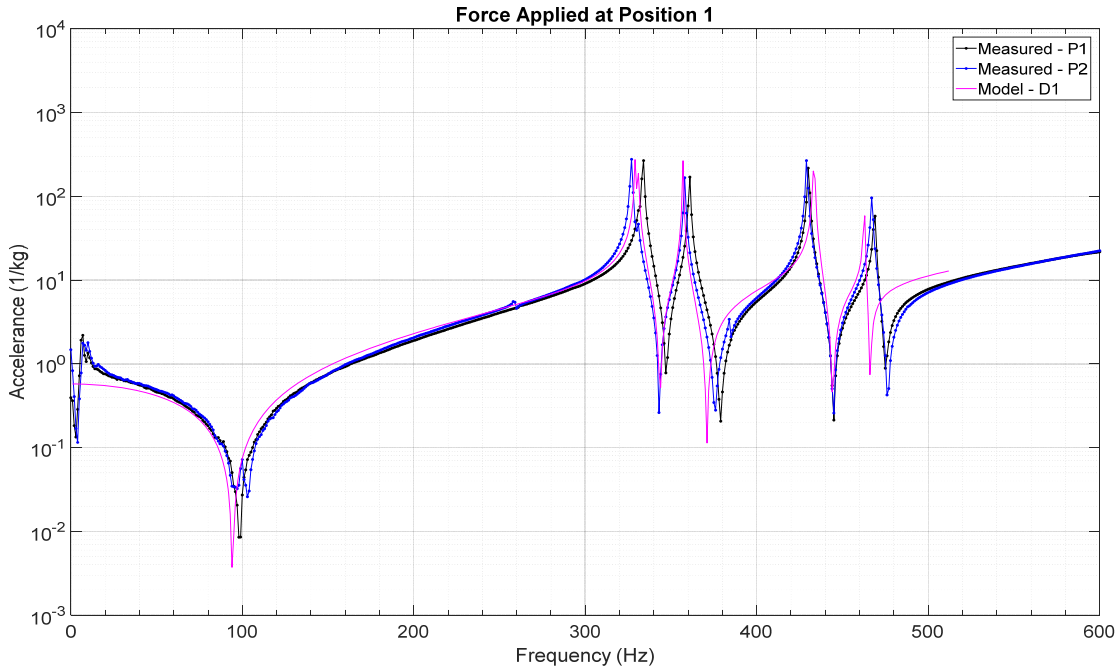

Figure 4B.1: Driving point accelerance for test pieces joined using both spot welds and structural adhesives and structurally damped tie constraint model (Model D1).

Figures 4B.3 and 4B.4 focus on the high frequency response at position 1 and 6, respectively. They show that around 330 Hz it is difficult for the model to match the measured data. More intriguing is the fact that the two physically measured results do no match. A frequency step analysis revealed that the part has two natural frequencies very close to each other, at 329 Hz and 330 Hz. The phenomenon seen is the result of nearly repeated modes.

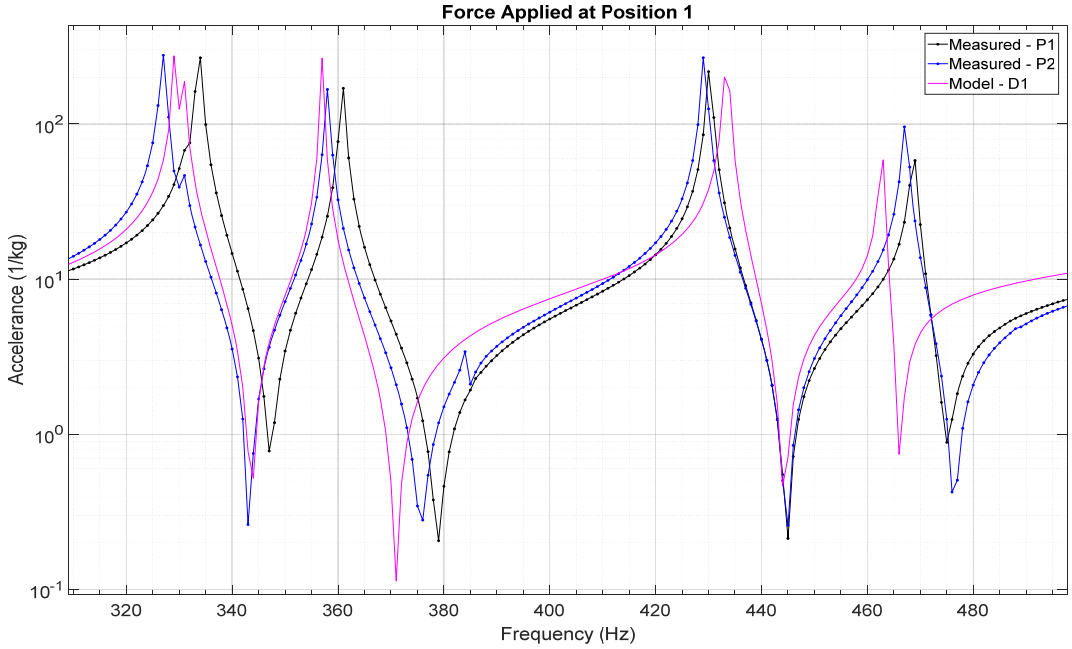

Figure 4B.3: Driving point accelerance for 320 Hz to 480 Hz range, for test pieces joined using both spot welds and structural adhesives and structurally damped tie constraint model (Model D1).

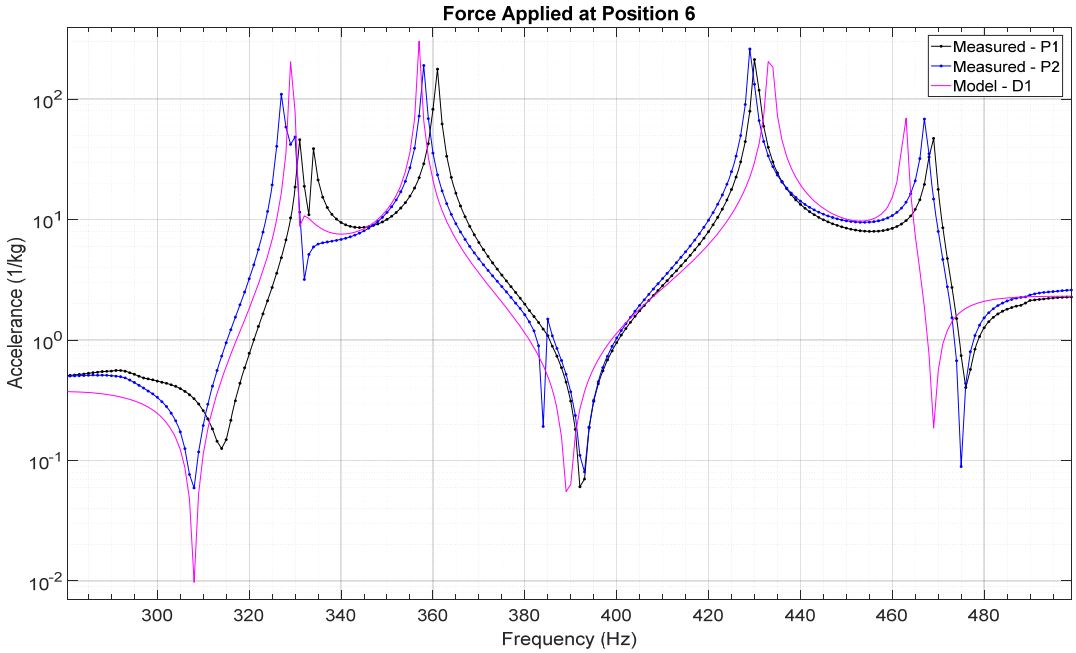

Figure 4B.4: Cross point accelerance for 320 Hz to 480 Hz range, for test pieces joined using both spot welds and structural adhesives and structurally damped tie constraint model (Model D1).

4C. Frequency Domain – Spot Weld Only Model

While all the models of double hat sections joined using spot welds and structural adhesives used a tie constraint between the flanges of the hat sections, all the models of double hat sections joined using only spot welds used Abaqus mesh independent fasteners to represent spot welds. These mesh independent fasteners are located by geometrically defined points and the displacement and rotation of each fastener is coupled, at the attachment points, to nearby nodes using a distributed constraint (Dassault Systèmes 6.14, 35.3.4).

One clear identifier of the need for spot weld modeling instead of continuing the use of a tie constraint was the different peak response observed and described in Chapter 2. Second, a physical inspection of the part 3, which is connected using only spot welds, revealed that there are intermittent areas of contact and no contact. This is shown in Figure 4C.1.

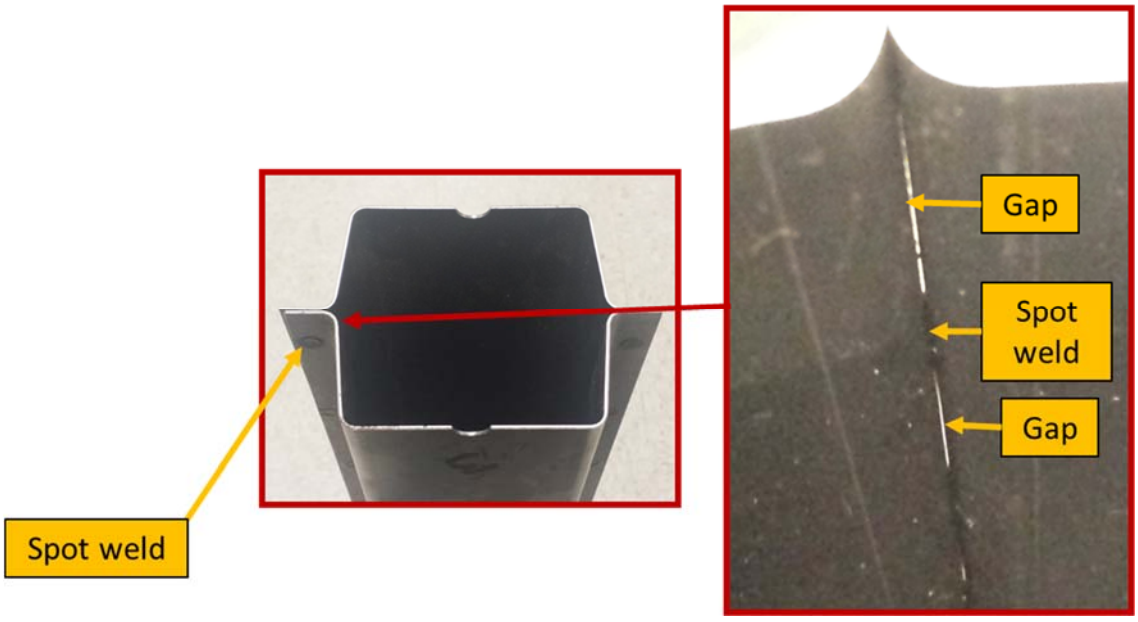

Figure 4C.1: Double hat section joined using only spot welds. Photo courtesy of Dr. Scott Noll.

A tie constraint would not make physical sense because the flanges are not rigidly connected at every point. The spot welds were modeled in Abaqus by creating two different connections for each physical connection. This required the creation of two sets of attachment points, which are the center points of a circle of a specified influence radius for that connection. Figure 4C.2 shows the positioning of the spot weld attachments, while Figure 4C.3 shows a close up of one spot weld to clearly show that two attachments create one spot weld. There are a total of 32 spot welds in the model, 16 on each flange. The attachments points were created by specifying 16 points, offset 7.5 mm either end of the hat section, and offset a set distance from the flange edge depending on whether it was a rigid connection (5 mm offset from edge) or damped connection (7.5 mm offset from edge).

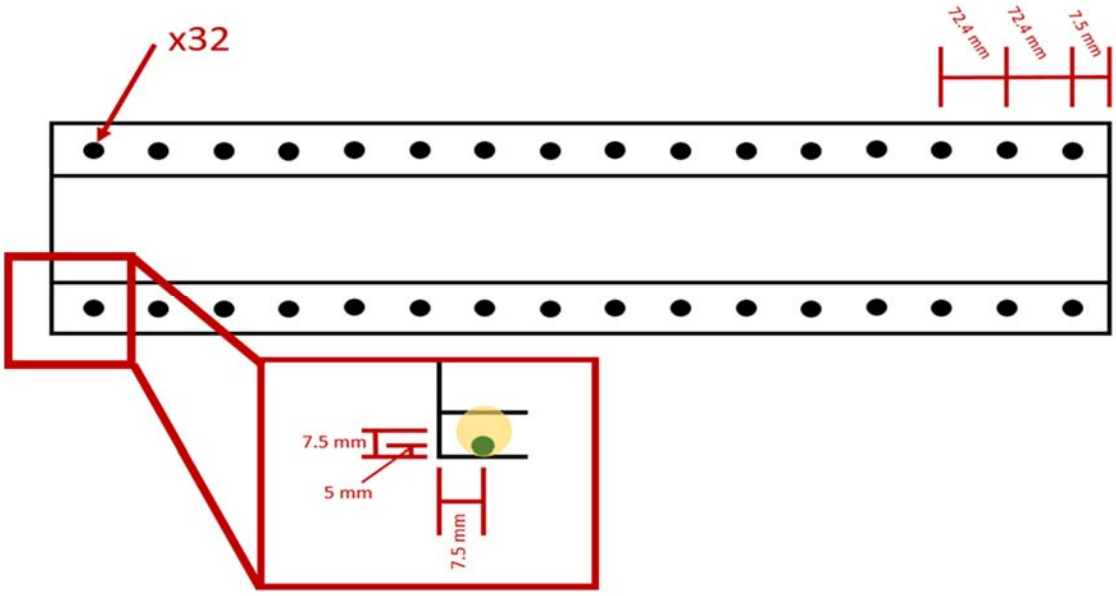

Figure 4C.2: Top view schematic of double hat section showing positioning of modeled spot welds. Key: (green circle) spot weld/rigid connection; (yellow circle) damped connection.

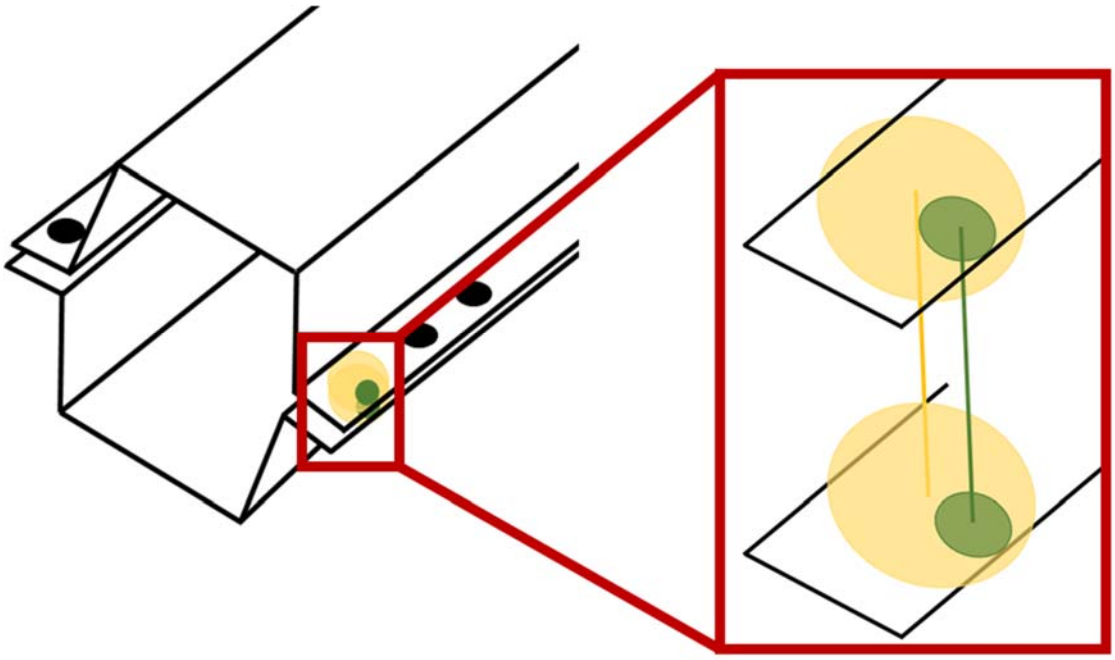

Figure 4C.2: 3D schematic of double hat section showing detailed model of a single spot weld. Key: (green circle) spot weld/rigid connection; (yellow circle) damped connection.

The spot weld model consisted of a rigid connection with an influence radius of 5 mm that was placed right against the outer edges of the flanges. This was because a visual inspection of the parts revealed the majority of the spot welds were closer to outside of the flanges than the middle of the flanges and that they had a 10 mm diameter. The second component of the spot weld model consisted of a damped connection with an influence radius of 10 mm in order to surround the rigid connection and were located in the center of the flanges. Table 4C.1 summarizes the Abaqus inputs for the mesh-independent fasteners.

Table 4C.1: Summary of mesh independent fastener inputs

Mesh Independent Fasteners	
Type:	Discrete
Coupling type:	Continuum distributing
Constrained DOF:	All
Weighting method	Uniform
Damping	
Definition:	Linear
Force:	F2 (y-direction)
Coupling:	Uncoupled
Use frequency-dependent data:	Model dependent
Data:	Model dependent

The first model created for capturing the frequency response of a double hat section joined using only spot welds consisted of material damping (the 0.00128 structural damping factor), rigid spot weld connections, and frequency dependent viscous damping (structural damping) in the damped spot weld connection (Model D2). Damping was applied in the y-direction, as defined in Figure 4C.4, due to the localized relative motion observed in the mode shapes at the lower frequencies being primarily in the y-direction. The direction of damping application was later confirmed when 100 times as much damping in the x-direction and the z-direction and no effect on the magnitude of the peaks was observed.

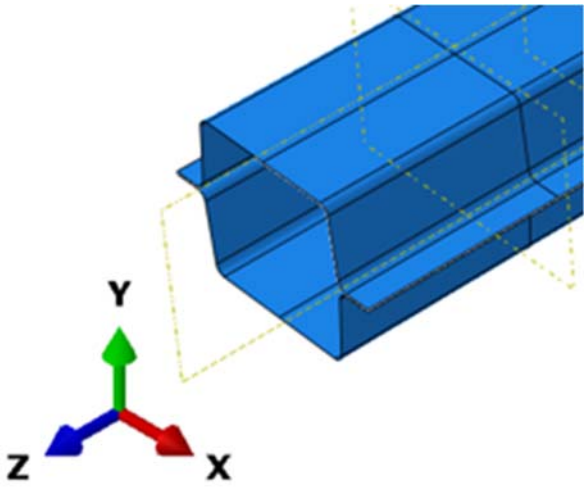

Figure 4C.4: 3D schematic of double hat section showing orientation of model in Abaqus.

In order to having a starting point for calculating the frequency dependent coefficients a static analysis was run. A single hat model was used. A 1 N force was applied to a single node while the flanges were fixed. The deflection of the single node was recorded and used to determine the part's stiffness as shown in Equation 4C.1. The part's stiffness is represented by the stiffness constant, k. The applied force is represented by F_y because it was applied in the negative y-direction and δ_y represent the deflection in the y-direction. Structural damping can be represented by an equivalent viscous damping coefficient, c_{eq} (Meirovitch, 1986). This coefficient determined by a relationship between the structural damping factor, γ, the stiffness constant, k, and the natural frequency, ω, in rad/s. The structural damping equivalent viscous damping coefficient was calculated for frequencies between 50 Hz and 500 Hz increments of 50 Hz. Equation 4C.2 shows this calculation at 50 Hz and Figure 4C.5 is a graph of the range of damping coefficient values.

$$k = \frac{F_y}{\delta_y} = \frac{1\ N}{0.00143\ mm} \approx 700 \frac{N}{mm} \tag{4C.1}$$

$$c_{eq} = \frac{\gamma * k}{\omega} = \frac{\gamma * k}{2 * \pi * f} = \frac{15 * 700\ \frac{N}{mm}}{2 * \pi * 50\ Hz} = 33.4\ \frac{N * s}{mm} \tag{4C.2}$$

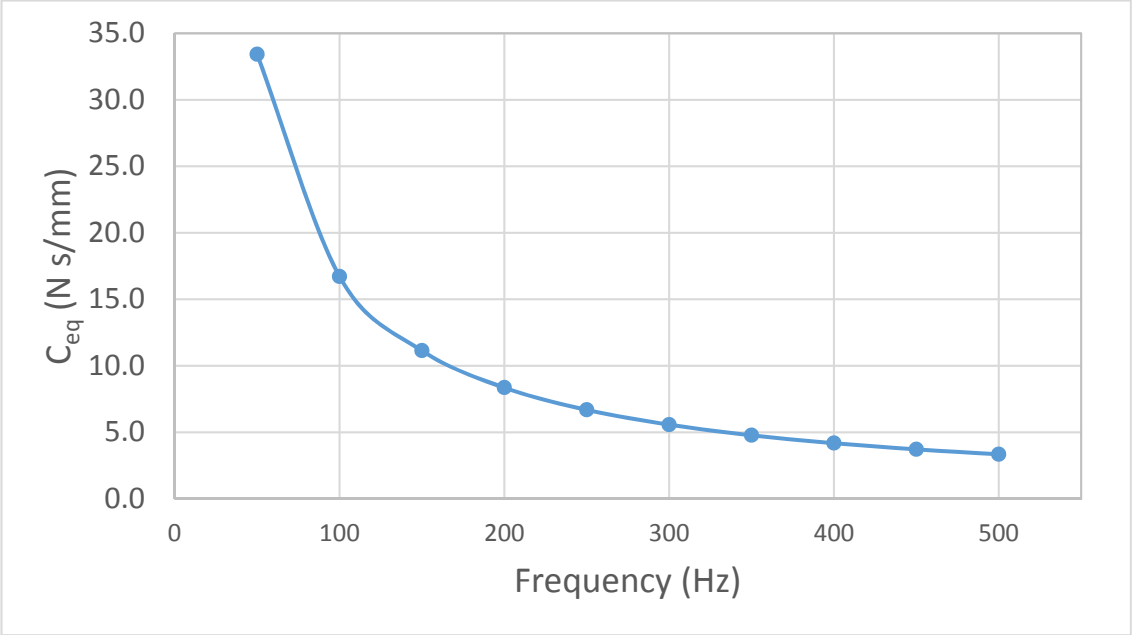

Figure 4C.5: Structural damping equivalent viscous damping coefficients over 50 Hz to 500 Hz range.

To find the structural damping factor, γ, an iterative approach was taken with the steady-state, dynamic Abaqus solutions and compared the magnitude of the frequency response function to the measured data form part 3. There was no visible effect of connection damping on the higher frequency, those greater than 400 Hz, peak responses. Visible distinctions between models could be observed in the peak response between 250 Hz and 350 Hz, so the effects of different structural damping factors were discernable. The structural damping factor was determined to be 15 and is unitless. Typically a structurally damping factor is a value between 0 and 1. Since both variables in the numerator of

Equation 4C.2 are unknown, the exact structural damping factor and stiffness values are unknown. The result of multiplying the structural damping factor and stiffness, which 10,500 N/mm, is what is known. With this definition for structural damping, the percent difference, at both positon 1 and 6, between Model D2 natural frequencies and part 3 measured natural frequencies was limited to 1.4%. The max percent difference for magnitude of accelerance was limited to 38.8%. Figure 4C.6 shows the iterative process at the driving point (position 1).

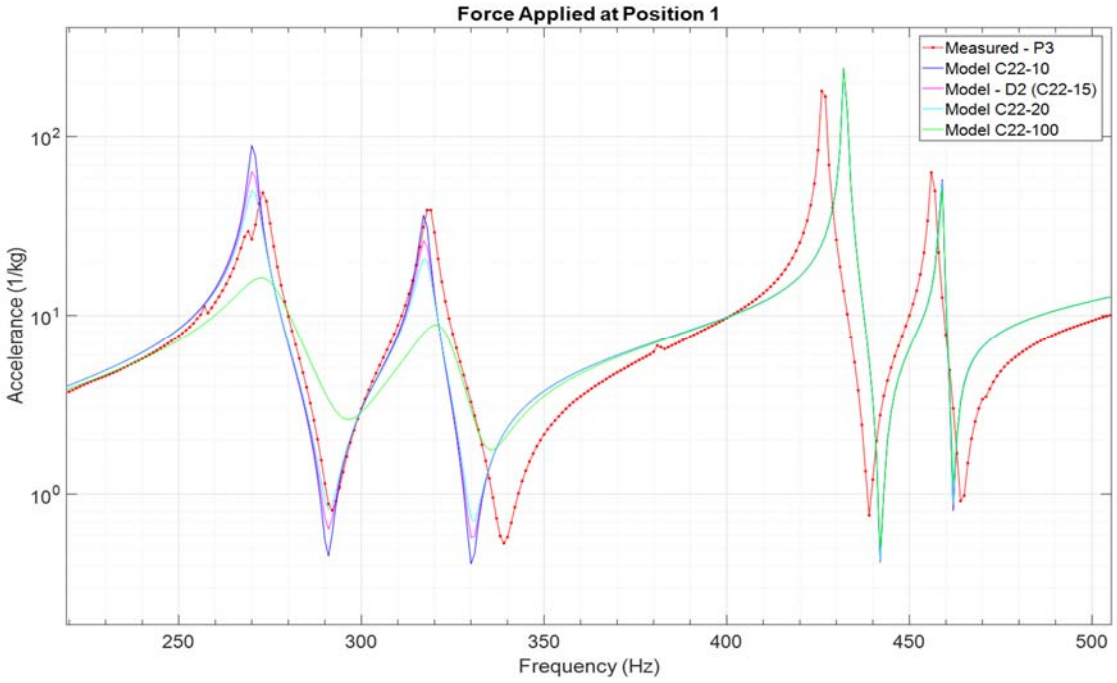

Figure 4C.6: Driving point accelerance for test pieces joined usin only spot welds and structurally damped spot weld connections models.

The next question was whether viscous damping alone, a single coefficient that is not frequency dependent, would be able to capture the damping phenomena. Again damping was applied in the y-direction, but with a single damping coefficient (Model D3). Different damping coefficients were iteratively tested using points from the line graphed

in Figure 4C.5. Again, there was no visible effect of connection damping on the higher frequency, those greater than 400 Hz, peak responses Visible distinctions between models could be observed in the peak response between 250 Hz and 350 Hz, so the effects of different structural damping factors were discernable. The viscous damping coefficient was determined to be 5.6 N s/mm. With this viscous damping coefficient, the percent difference, at both positon 1 and 6, between Model D3 natural frequencies and part 3 measured natural frequencies was limited to 1.4%. The maximum percent difference for magnitude of accelerance was limited to 42.8%. Figure 4C.7 shows the results of the iterative process at the driving point (position 1).

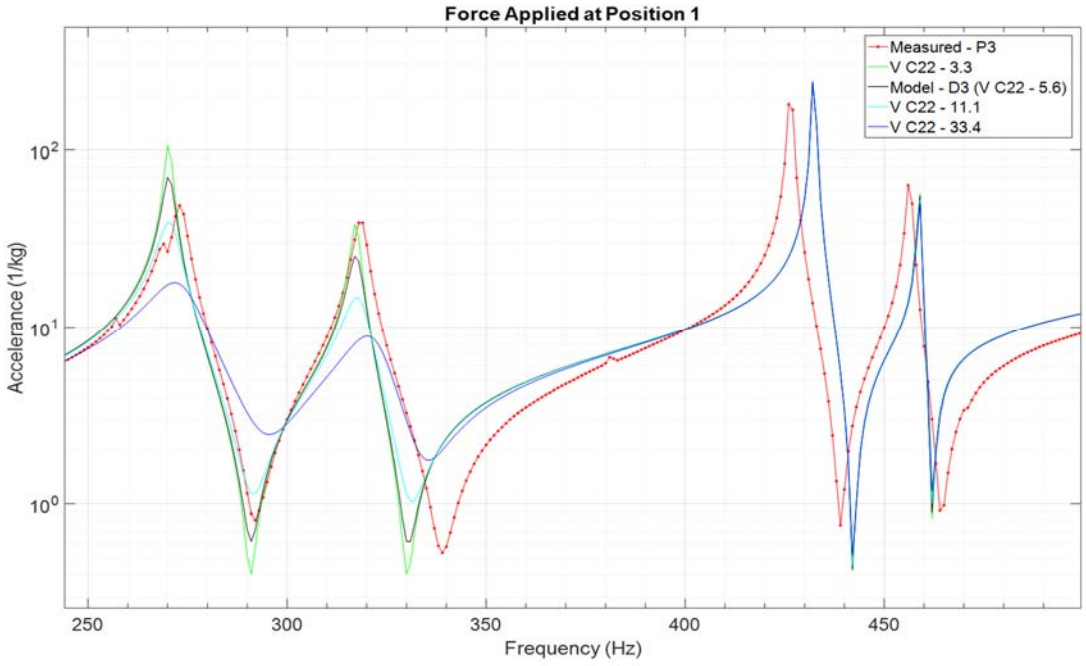

Figure 4C.6: Driving point accelerance for test pieces joined using only spot welds and viscously damped spot weld connections models.

The linearized connection damping definition, viscous damping instead of structural damping, likely was effective as the modes were concentrated in the 300 Hz to

500 Hz range which is a relatively level region of damping, refer to Figure 4C.5. For a more complex structure that contains vibratory modes over a wider range of frequencies, it would likely be necessary to use a structural damping definition; however, further investigation is required.

Chapter 5: Conclusion

The first key result from this research was the finding the necessity of the incorporation of damping into the finite element models. Table 6.1 summarizes the different damping models analyzed in this research. The second key result was identifying the different damping mechanism present when there is no structural adhesive used to join the two single hat sections. This was addressed by modeling individual spot welds.

Table 6.1: Summary of damping models. Key: (X) not included; (✓) included

Domain	Model Name	**Damping Models**			
		Material Property		Connection Properties	
		Rayleigh Damping	Structural Damping	Frequency Dependent Viscous Damping (Analogous to structural Damping)	Viscous Damping
Frequency	**D0**	X	X	X	X
	D1	X	✓	X	X
	D2	X	✓	✓	X
	D3	X	✓	X	✓

Model D1 was validated in the frequency domain for parts 1 and 2, or those double hat sections that were joined using a combination of structural adhesives and spot welds.

Models D2 and D3 were shown to be very similar and validated in the frequency domain for part 3, or the double hat section that was joined using only spot welds. These models showed that it is critical to include damping in the modeling of the spot welds (there is damping in addition to the material damping) in order to capture the frequency response of part 3.

In summary, frequency domain analysis results show that the double hat section specimens used in this study, which were joined with structural adhesives and spot welds, can be idealized as having rigid connections with light material damping. Conversely, the double hat section specimen joined via spot welds alone exhibits significantly higher damping due to dissipation mechanisms within the interface.

Chapter 6: Future Work

In the time domain a dynamic explicit step was used to obtain the impulse response of the system (Abaqus, 2014). Within this step the bulk viscosity damping parameters were set equal to zero. S4R elements were used because Abaqus only offers linear explicit elements (Abaqus, 2014). Given that quadratic elements were used in every other solution step it was expected that a finer mesh would be required for convergence. The time period of the step was 0.003 second when analyzing the initial peak response in the time domain. While the time period was 0.4 seconds when the results were converted to the frequency response function using MATLAB's fast Fourier transform function (MATLAB, 2016). The field output request was based on frequency and used evenly spaced time intervals. The timing was set to output at exact times. The number of intervals was 122 or 16383 for

the 0.003 seconds and 0.4 seconds time periods, respectively. The number of intervals was based on the experimental sampling frequency of 40960 Hz.

6A. Time Domain – Rayleigh Damping

Structural damping cannot be applied to a material in time domain analyses as this leads to non-causal behavior. Therefore, equivalent Rayleigh damping parameters were determined in the frequency domain through an iterative procedure. Rayleigh damping is a type of damping where $\mathbf{C}=\alpha\mathbf{M}+\beta\mathbf{K}$ and **C**, **M**, and **K** are the damping, mass, and stiffness matrices, respectively (Meirovitch, 1986). It is defined by the two Rayleigh damping factors, α and β, which are proportional to mass and stiffness respectively (Dassault Systemes 6.14, 26.1.1). The quality factor, Q, was determined using part 2's measured frequency response.

Equation 6A.1 shows how the Q factor can be determined using the frequency response function. In this equation f_0 is the natural frequency in Hz, f_2 is the frequency value in Hz higher than f_0 that corresponds to an amplitude 3 dB below the peak amplitude, and f_1 is the frequency value in Hz lower than f_0 that corresponds to an amplitude 3 dB below the peak amplitude. The damping ratio, ξ, was determined using Eqn. 6A.2. This procedure was followed at two peak locations, 327 Hz and 467 Hz, so that Eqn. 6A.4 and 6A.5 represented two equations with two unknowns, α and β. The Q factor at 327 Hz was labeled as Q_1 and the Q factor at 467 Hz was labeled as Q_2. The natural frequencies in Hz, used to find the Q factor, are related to the natural frequencies used in Eqn. 6A.4 and 6A.5 by Eqn. 6A.3. The damping ratios, ξ_1 and ξ_2, were iterated on using an Abaqus steady-state dynamics, direct solution step, described in Chapter 4, using peak magnitude as the updating parameter.

$$Q_1 = \frac{f_0}{f_2 - f_1} \tag{6A.1}$$

$$\xi_1 = \frac{1}{2Q_1} \tag{6A.2}$$

$$\omega_1 = 2\pi f_1 \tag{6A.3}$$

$$2\xi_1\omega_1 = \alpha + \beta{\omega_1}^2 \tag{6A.4}$$

$$2\xi_2\omega_2 = \alpha + \beta{\omega_2}^2 \tag{6A.5}$$

The Rayleigh damping was determined to be defined by α equal to 1.02 s^{-1} and β equal to 3.51E-07 s. The difference between Model D1 and the Rayleigh damping model (Model D4), shown in Figure 6A.1, is nearly indiscernible with a maximum difference in amplitude of 4.4%, which is well within the experimental part-to-part variability. The α and β inputs were then applied in the time domain analysis in combination with a tie constraint along the two double hat sections' flanges.

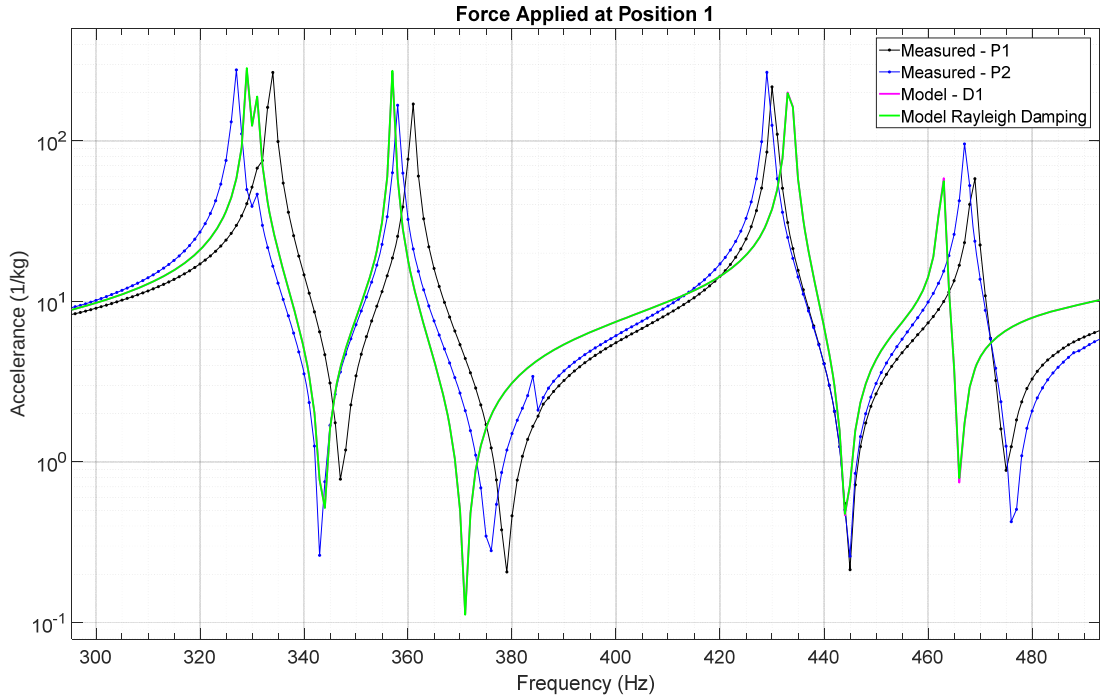

Figure 6A.1: Driving point accelerances for 320 Hz to 480 Hz range, for test pieces joined using both spot welds and structural adhesives, structurally damped tie constraint model (Model D1), and Rayleigh damped tie constraint model. *Note that the Rayleigh damping results almost exactly match the structural damping results.

6B. Time Domain – Spot Weld and Structural Adhesive Model

Model D4 used a tie constraint and Rayleigh damping. When using the converged mesh, described in detail in Chapter 4, the initial response, first 0.003 sec, was not captured by the model. There was visual improvement of the initial response when a global mesh size of 5 mm was used, and again when a global mesh size of 2.5 mm was used. The initial response for Model D4 showed numerical instability after 0.25 sec.

6C. Time Domain – Spot Weld Only Model

Model D5 used the spot weld connections used in Model 2 and Rayleigh damping. The same visual improvement was observed when moving from the mesh described in Chapter 4 to a global mesh size of 5 mm and again when moving to a global mesh size of

2.5 mm. The magnitude of the frequency response was obtained from the Abaqus dynamic, explicit step using MATLAB's fast Fourier transform function and a 5 mm global mesh (MATLAB, 2016). Unexpected numerical damping was observed when plotting the frequency response function. The first two peaks were lower than what was physically observed during the experiments.

Another issue theses graphs brought to light was the fact that the mesh, which had converged for the tie constraint in the frequency domain, had not converged for the model with spot welds. The first two peaks were shifted to the left more than what was physically observed. In the future, it is key to make sure the mesh has converged for the spot welds. Abaqus' mesh independent fasteners are defined independent of the mesh but the coupling constraint used to enforce the fastener properties does depend on the mesh (Dassault Systèmes 6.14, 35.3.4). Once the mesh has converged the location of the spot welds can be iterated on and the same iterative procedure described in Chapter 5 can be used to find the correct structural damping factor, γ.

6D. Time Domain – Summary

An initial investigation into time domain analyzes demonstrated that results from the frequency domain could not be directly translated to the time domain formulation. Future work is needed to address the challenges of numerical stability, numerical damping, and element type sensitivity due to the differences in linear versus quadratic shape functions. It is recommended that future work begin with a mesh convergence study for the spot weld model and identification of suitable damping parameters for the dynamic explicit solution step.

References

Abaqus CAE (6.14) [Computer Software]. (2014). Providence, RI: Dassault Systèmes Simulia Corp.

Chou, C. C., Le, J., Chen, P., & Bauch, D. J. (2001, June 6). Development of CAE simulated crash pulses for airbag sensor algorithm/calibration in frontal impacts, SAE Technical Paper 2001-06-0059

Dassault Systèmes, Abaqus 6.14, Abaqus Analysis User's Guide, 26.1.1 Material Damping. Retrieved from http://www-archive.abe.iastate.edu/abaqus/Documentation/docs/v6.14/

Dassault Systèmes, Abaqus 6.14, Abaqus Analysis User's Guide, 35.3.4 Mesh-independent fasteners. Retrieved from http://www-archive.abe.iastate.edu/abaqus/Documentation/docs/v6.14/

Ghassemieh, E. (2011, January 8). Materials in Automotive Application, State of the Art and Prospects, New Trends and Developments in Automotive Industry, Prof. Marcello Chiaberge (Ed.), InTech, DOI: 10.5772/13286. Available from: http://www.intechopen.com/books/new-trends-and-developments-in-automotive-industry/materials-in-automotive-application-state-of-the-art-and-prospects

Gibbs, N. (2015, October 20). How digital prototyping is cutting development time and costs for new models. *Automotive News Europe*. Retrieved from www.autonews.com/article/20151020/COPY01/310209965/how-digital-prototyping-is-cutting-development-time-and-costs-for-new-

LMS Test.Lab (15A) [Computer Software]. (2015). Munich, Germany: Siemens Product Lifecycle Management Software Inc.

MATLAB (R2016b) [Computer Software]. (September 7, 2016). Nadick, MA: The MathWorks, Inc.

Meirovitch, L. (1986). *Elements of Vibration Analysis* (Second ed.,pp. 71-73, 196-197). N.p.: McGraw-Hill Book Company.

National Highway Traffic Safety Administration (NHTSA). (n.d.). Air bags. Retrieved March 12, 2017, from https://www.nhtsa.gov/equipment/air-bags

NHTSA NVS, Vehicle Crash Test Database Test No. 9590 Camera No. 10 – Overhead Wide View Of Impact.avi [Screenshot from online video v0950c002.avi]. Retrieved April 7, 2017 from https://www-nrd.nhtsa.dot.gov

Pava, Milano. (2015). [Untitled image of Automobile body pillars]. Retrieved April 7, 2017 from https://commons.wikimedia.org

Pearly Huffman, J. (2011, June). The physics of: Airbags. In *Car and Driver*. Retrieved March 12, 2017, from http://www.caranddriver.com/features/the-physics-of-airbags-feature

Statistics Department National Safety Council. (2016, January 13). NSC Motor Vehicle Fatality Estimates. Retrieved March 12, 2017, from http://www.nsc.org/NewsDocuments/2016/mv-fatality-report-1215.pdf

Stutzler, F. J., Chou, C. C., Le, J. and Chen, Ping, Development of CAE-based crash sensing algorithm and system calibration, SAE Technical Paper 2003-01-0509

[Untitled image of air bags and air curtains]. Retrieved April 7, 2017 from http://www.chicagonow.com

[Untitled image of airbag control unit and remote sensor]. Retrieved April 7, 2017 from http://www.careers.webdev.trw.com

[Untiled image of BMW 7-series body-in-white]. Retrieved April 7, 2017 from http://www.compositesworld.com

Appendix I: Mesh Convergence

IA. Global Mesh Convergence Study

A mesh convergence study, using frequency response, was performed to identify the minimum size and distribution of elements to adequately capture results. Various element types and sizes were analyzed, but the model setup shown in Table IA.1 remained constant throughout the entire convergence study.

Table IA.1:Mesh convergence model setup

Material: Steel	
Density (tonne/mm3):	7.85E-09
Mechanical	
Elasticity:	Elastic
Type:	Isotropic
Young's Modulus (MPa):	200000
Poisson's Ratio:	0.32
Section: Shell	
Section integration:	during analysis
Thickness (mm):	1.4
Thickness integration rule:	Simpson
Thickness integration points:	5
Constraint	
Type:	tie
Master surface:	bottom side of flange from top Hat-Section
Slave surface:	top side of flange from bottom Hat-Section
Step: Frequency	
Eigensolver:	Lanczos

Initially, the global element size was adjusted as shown in Table IA.2. The frequency step requested the first 10 eigenvalues and standard linear quadrilateral quad-dominated (S4R) elements were used. The first 6 eigenvalues are zero because they represent rigid body motion for each DOF. Table IA.2 shows the first four, nonzero, natural frequencies obtained for various global element sizes. For convergence based on enforcing a percent change of 1% or less the model has converged for approximate global elements sizes of 5 mm and 10 mm. Table IA.3 provides visualization of the various mesh sizes evaluated.

Table IA.2: Summary of Global Size Mesh Convergence

Total # of elements	19360	6160	1980	784	252
Approximate Global Size (mm)	5	10	20	40	80
f_7 (Hz)	253	254	260	286	363
f_8 (Hz)	253	255	260	286	364
f_9 (Hz)	328	330	338	375	429
f_{10} (Hz)	329	331	339	376	439
Percent Change =absolute($100*(f_2-f_1)/f_1$)					
f_7 (Hz)	0.56	2.24	9.06	21.09	-
f_8 (Hz)	0.53	2.22	9.02	21.29	-
f_9 (Hz)	0.59	2.50	9.82	12.56	-
f_{10} (Hz)	0.59	2.48	9.73	14.46	-

Table IA.3: Visual Mesh Global Mesh Size

Total Number of Elements	Global Size (mm)	Mesh
19360	5	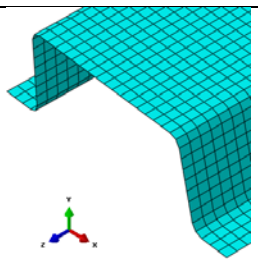
6160	10	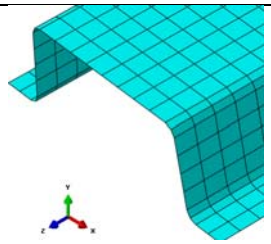
2774	15	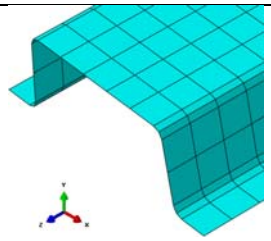
1980	20	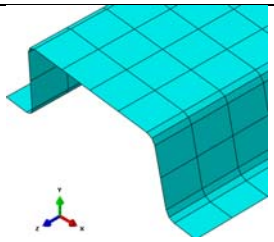
784	40	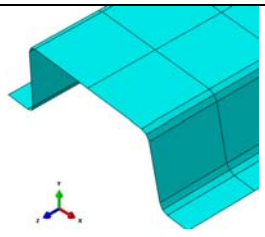

252	80	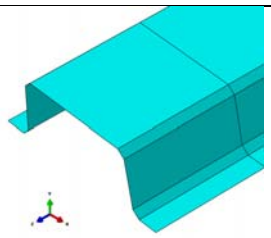

IB. Z-direction Convergence Study

Then the global mesh was kept constant while the number of elements along the z-axis, or the length of the b-pillar, were adjusted. The frequency step requested the first 10 eigenvalues and standard linear quadrilateral quad-dominated (S4R) elements were used. This was done for a global mesh size of 20 mm. Table IB.1 shows the first four, nonzero, natural frequencies obtained for the various mesh configuration. This results present a false sense of convergence to higher natural frequencies. The frequency values are not changing significantly because a global mesh size of 20 mm across the b-pillar's cross-section is too course. It will be shown in the following section that the model is more sensitive across its cross-section than along it length.

Table IB.1: Summary of Z-direction Mesh Convergence

Total # of Elements	15840	7920	3960	1980
Approximate Global Size (mm)	20	20	20	20
Z-dir Size	2.5	5	10	20
f_7 (Hz)	260	260	260	260
f_8 (Hz)	260	260	260	260
f_9 (Hz)	338	338	338	338
f_{10} (Hz)	339	339	339	339
Percent Change =absolute($100*(f_2-f_1)/f_1$)				
f_7 (Hz)	0.01	0.02	0.02	-
f_8 (Hz)	0.00	0.00	0.00	-
f_9 (Hz)	0.00	0.00	0.00	-
f_{10} (Hz)	0.00	0.00	0.00	-

IC. X-direction Convergence Study

Then the global mesh was kept constant while the number of elements along the x-axis, or the cross-section of the b-pillar, were adjusted. This was done for a global mesh size of both 20 mm, 40 mm, and 80 mm. The frequency step requested the first 16 eigenvalues and standard linear quadrilateral quad-dominated (S4R) elements were used. The same results were obtained when Explicit Quadrilateral Quad-dominated elements were used. The results from a global mesh size of 20mm are plotted in Figure IC.1. This figure provides visualization of the decreasing element size required for the convergence of higher natural frequencies. Table IC.1 provides visualization of the mesh refinement. All of the results for the first ten, nonzero, natural frequencies are shown in Tables IC.2 through IC.4. Here convergence has been defined as a percent change of 0.3% or less because this will result in less than 2 Hz error for frequencies of 600 Hz. These results

show that number of elements in the x-direction is more critical than the number of elements in the z-direction, because for each global element size the model has converged once the x-direction size is less than or equal to 2.5 mm. However, a new point of concern is the fact the natural frequencies converge to different values for different global mesh sizes. The accuracy of this model will be evaluated in the following section.

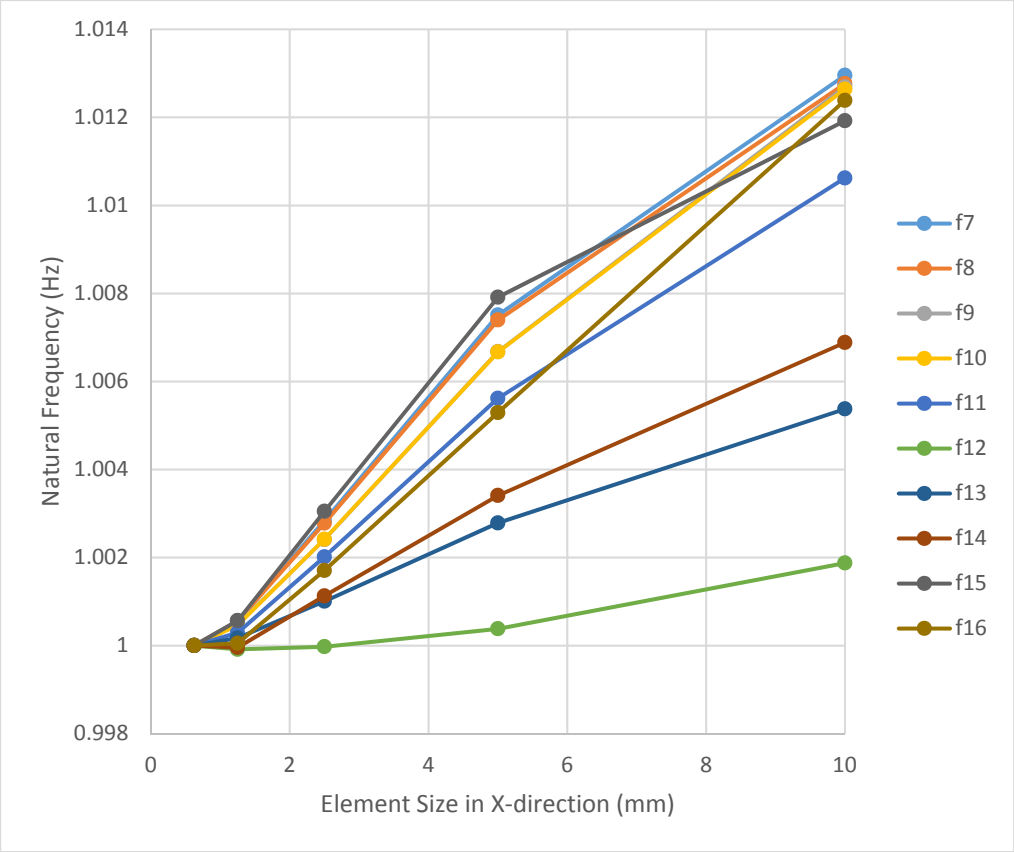

Figure IC.1: Summary of X-direction mesh Convergence with Global Size of 20mm

Table IC.1: Visual Mesh X-direction Mesh Size

Total Number of Elements	Global Size (mm)	X-Direction Size (mm)	Mesh
3080	20	10	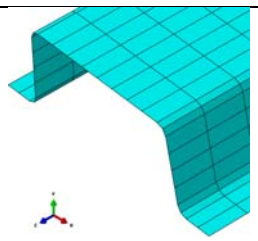
5040	20	5	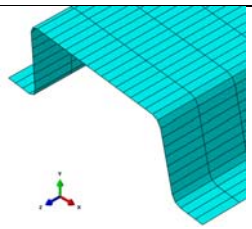
9520	20	2.5	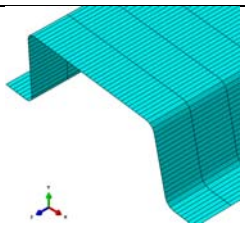
2464	40	10	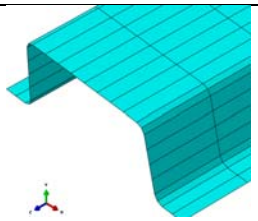

4704	40	5	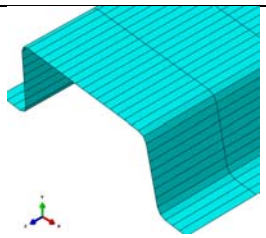
11648	40	2.5	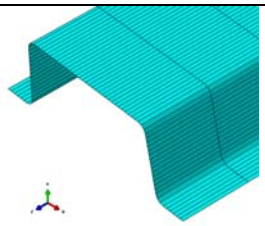

Table IC.2: Summary of X-direction Mesh Convergence with Global Size of 20mm

Total # of Elements	36960	18480	9240	4840	3080
Approximate Global Size (mm)	20	20	20	20	20
X-dir Size	0.625	1.25	2.5	5	10
f_7 (Hz)	251	251	252	253	254
f_8 (Hz)	251	252	252	253	255
f_9 (Hz)	326	326	326	328	330
f_{10} (Hz)	327	327	328	329	331
f_{11} (Hz)	352	353	353	354	356
f_{12} (Hz)	383	383	383	383	383
f_{13} (Hz)	426	426	426	427	428
f_{14} (Hz)	456	456	457	458	459
f_{15} (Hz)	469	469	470	473	475
f_{16} (Hz)	608	608	609	611	616
Percent Change =absolute($100*(f_2-f_1)/f_1$)					
f_7 (Hz)	0.06	0.23	0.46	0.54	-
f_8 (Hz)	0.06	0.22	0.46	0.53	-
f_9 (Hz)	0.05	0.19	0.42	0.59	-
f_{10} (Hz)	0.05	0.19	0.42	0.59	-
f_{11} (Hz)	0.03	0.17	0.36	0.50	-
f_{12} (Hz)	0.01	0.01	0.04	0.15	-
f_{13} (Hz)	0.02	0.08	0.18	0.26	-
f_{14} (Hz)	0.00	0.12	0.23	0.35	-
f_{15} (Hz)	0.06	0.25	0.48	0.40	-
f_{16} (Hz)	0.01	0.17	0.36	0.70	-

Table IC.3: Summary of X-direction Mesh Convergence with Global Size of 40mm

Total # of Elements	18816	9408	4704	2464	1568
Approximate Global Size (mm)	40	40	40	40	40
X-dir Size	0.625	1.25	2.5	5	10
f_7 (Hz)	251	251	252	253	254
f_8 (Hz)	251	252	252	253	255
f_9 (Hz)	326	326	326	328	330
f_{10} (Hz)	327	327	327	329	331
f_{11} (Hz)	352	352	353	354	356
f_{12} (Hz)	383	383	383	383	384
f_{13} (Hz)	426	426	427	427	428
f_{14} (Hz)	458	457	458	459	460
f_{15} (Hz)	470	470	471	473	475
f_{16} (Hz)	610	610	611	613	617
Percent Change =absolute($100*(f_2-f_1)/f_1$)					
f_7 (Hz)	0.06	0.23	0.46	0.54	-
f_8 (Hz)	0.06	0.22	0.46	0.53	-
f_9 (Hz)	0.05	0.19	0.42	0.59	-
f_{10} (Hz)	0.04	0.20	0.43	0.59	-
f_{11} (Hz)	0.00	0.17	0.36	0.49	-
f_{12} (Hz)	0.04	0.01	0.03	0.14	-
f_{13} (Hz)	0.01	0.08	0.18	0.26	-
f_{14} (Hz)	0.09	0.08	0.21	0.34	-
f_{15} (Hz)	0.04	0.24	0.48	0.40	-
f_{16} (Hz)	0.08	0.13	0.35	0.72	-

Table IC.4: Summary of X-direction Mesh Convergence with Global Size of 80mm

Total # of Elements	9408	4704	2352	1232	784
Approximate Global Size (mm)	80	80	80	80	80
X-dir Size	0.625	1.25	2.5	5	10
f_7 (Hz)	251	251	252	253	254
f_8 (Hz)	251	252	252	253	255
f_9 (Hz)	326	326	326	328	330
f_{10} (Hz)	326	326	327	328	330
f_{11} (Hz)	352	351	352	353	355
f_{12} (Hz)	386	385	385	385	386
f_{13} (Hz)	428	428	429	429	430
f_{14} (Hz)	461	460	460	461	462
f_{15} (Hz)	472	472	473	475	477
f_{16} (Hz)	613	611	612	614	620
Percent Change =absolute($100*(f_2-f_1)/f_1$)					
f_7 (Hz)	0.06	0.24	0.46	0.54	-
f_8 (Hz)	0.06	0.22	0.46	0.53	-
f_9 (Hz)	0.05	0.19	0.42	0.59	-
f_{10} (Hz)	0.04	0.20	0.43	0.59	-
f_{11} (Hz)	0.06	0.15	0.35	0.49	-
f_{12} (Hz)	0.12	0.05	0.00	0.13	-
f_{13} (Hz)	0.02	0.06	0.18	0.27	-
f_{14} (Hz)	0.30	0.01	0.17	0.34	-
f_{15} (Hz)	0.01	0.22	0.48	0.41	-
f_{16} (Hz)	0.24	0.10	0.38	0.83	-

ID. X-direction Convergence Study with Quadratic Elements

Again the global mesh was kept constant while the number of elements along the x-axis, or the cross-section of the b-pillar, were adjusted. This was done for a global mesh size of both 20 mm, 40 mm, and 80 mm. The frequency step requested the first 16

eigenvalues and standard quadratic quadrilateral quad-dominated (S8R) elements were used. The results for the first ten, nonzero, natural frequencies are shown in Tables AD.1 through AD.3. Here convergence has again been defined as a percent change of 0.3% or less. Here there is confidence in the accuracy of the model because the natural frequencies converge to the same values for various global element size configurations. Indeed, this was expected and quadratic elements are known to have better accuracy than linear elements. A new question arises due to the fact that the natural frequencies have already converged for all of the configurations. That is, what is the least number of elements for which the simulation results are still converged.

Table ID.1: Summary of X-direction Mesh Convergence with Global Size of 20mm

Total # of Elements	36960	18480	9240	4840	3080
Approximate Global Size (mm)	20	20	20	20	20
X-dir Size	0.625	1.25	2.5	5	10
f_7 (Hz)	251	251	251	251	251
f_8 (Hz)	251	251	251	251	251
f_9 (Hz)	326	326	326	326	326
f_{10} (Hz)	327	327	327	327	327
f_{11} (Hz)	352	352	352	352	352
f_{12} (Hz)	382	382	383	383	383
f_{13} (Hz)	425	425	425	425	425
f_{14} (Hz)	456	456	456	456	456
f_{15} (Hz)	469	469	469	469	469
f_{16} (Hz)	607	607	607	607	607
Percent Change =absolute($100*(f_2-f_1)/f_1$)					
f_7 (Hz)	0.00	0.01	0.01	0.01	-
f_8 (Hz)	0.00	0.00	0.00	0.00	-
f_9 (Hz)	0.00	0.00	0.00	0.00	-
f_{10} (Hz)	0.00	0.00	0.01	0.00	-
f_{11} (Hz)	0.00	0.00	0.01	0.00	-
f_{12} (Hz)	0.01	0.02	0.02	0.01	-
f_{13} (Hz)	0.00	0.01	0.01	0.00	-
f_{14} (Hz)	0.00	0.00	0.01	0.00	-
f_{15} (Hz)	0.00	0.00	0.01	0.00	-
f_{16} (Hz)	0.00	0.00	0.01	0.00	-

Table ID.2 Summary of X-direction Mesh Convergence with Global Size of 40mm

Total # of Elements	18816	9408	4704	2464	1568
Approximate Global Size (mm)	40	40	40	40	40
X-dir Size	0.625	1.25	2.5	5	10
f_7 (Hz)	251	251	251	251	251
f_8 (Hz)	251	251	251	251	251
f_9 (Hz)	326	326	326	326	326
f_{10} (Hz)	327	327	327	327	327
f_{11} (Hz)	352	352	352	353	353
f_{12} (Hz)	382	382	382	383	383
f_{13} (Hz)	425	425	425	425	425
f_{14} (Hz)	456	456	456	456	456
f_{15} (Hz)	469	469	469	469	469
f_{16} (Hz)	607	607	607	607	607
Percent Change =absolute($100*(f_2-f_1)/f_1$)					
f_7 (Hz)	0.00	0.01	0.02	0.02	-
f_8 (Hz)	0.00	0.00	0.01	0.01	-
f_9 (Hz)	0.00	0.00	0.01	0.00	-
f_{10} (Hz)	0.00	0.01	0.01	0.01	-
f_{11} (Hz)	0.00	0.01	0.01	0.01	-
f_{12} (Hz)	0.01	0.02	0.02	0.01	-
f_{13} (Hz)	0.00	0.01	0.01	0.00	-
f_{14} (Hz)	0.00	0.01	0.01	0.01	-
f_{15} (Hz)	0.00	0.00	0.01	0.01	-
f_{16} (Hz)	0.00	0.00	0.01	0.01	-

Table ID.3: Summary of X-direction Mesh Convergence with Global Size of 80mm

Total # of Elements	9408	4704	2352	1232	784
Approximate Global Size (mm)	80	80	80	80	80
X-dir Size	0.625	1.25	2.5	5	10
f_7 (Hz)	251	251	251	251	251
f_8 (Hz)	251	251	251	251	251
f_9 (Hz)	326	326	326	326	326
f_{10} (Hz)	327	327	327	327	327
f_{11} (Hz)	352	352	352	353	353
f_{12} (Hz)	382	382	382	383	383
f_{13} (Hz)	425	425	425	425	425
f_{14} (Hz)	456	456	456	456	456
f_{15} (Hz)	469	469	469	469	469
f_{16} (Hz)	607	607	607	608	608
Percent Change =absolute($100*(f_2-f_1)/f_1$)					
f_7 (Hz)	0.01	0.01	0.02	0.02	-
f_8 (Hz)	0.00	0.00	0.01	0.01	-
f_9 (Hz)	0.00	0.01	0.02	0.01	-
f_{10} (Hz)	0.01	0.02	0.03	0.02	-
f_{11} (Hz)	0.01	0.02	0.03	0.02	-
f_{12} (Hz)	0.01	0.02	0.02	0.01	-
f_{13} (Hz)	0.00	0.01	0.01	0.01	-
f_{14} (Hz)	0.00	0.01	0.02	0.01	-
f_{15} (Hz)	0.00	0.01	0.01	0.01	-
f_{16} (Hz)	0.01	0.03	0.04	0.03	-

IE. Z-direction Convergence Study with Quadratic Elements Fewest Elements

Again the global mesh was kept constant while the number of elements along the z-axis, or the length of the b-pillar, were adjusted. To maintain a constant x-direction element size it was determined that the maximum x-direction element size is 5mm. So the global mesh size used was 5 mm. The z-direction element size was evaluated at 20, 40, 80, and 160 mm. The frequency step requested the first 16 eigenvalues and standard quadratic quadrilateral quad-dominated (S8R) elements were used. The results for the first ten, nonzero, natural frequencies are shown in Table IE.1. Here convergence has again been defined as a percent change of 0.3% or less. From Table IE.1 it is shown, that with using the maximum x-direction element size, the minimum z-direction size required for convergence is 80mm resulting in a minimum of 1232 total elements.

Table IE.1: Summary of Z-direction Mesh Convergence with Global Size of 5mm

Total # of Elements	4840	2464	1232	616
Approximate Global Size (mm)	20	40	80	160
X-dir Size	5	5	5	5
f_7 (Hz)	251	251	251	251
f_8 (Hz)	251	251	251	251
f_9 (Hz)	326	326	326	326
f_{10} (Hz)	327	327	327	327
f_{11} (Hz)	352	353	353	352
f_{12} (Hz)	383	383	383	382
f_{13} (Hz)	425	425	425	425
f_{14} (Hz)	456	456	456	459
f_{15} (Hz)	469	469	469	468
f_{16} (Hz)	607	607	608	621
Percent Change =absolute($100*(f_2-f_1)/f_1$)				
f_7 (Hz)	0.01	0.00	0.00	-
f_8 (Hz)	0.01	0.00	0.05	-
f_9 (Hz)	0.01	0.01	0.02	-
f_{10} (Hz)	0.01	0.04	0.02	-
f_{11} (Hz)	0.01	0.01	0.13	-
f_{12} (Hz)	0.01	0.02	0.05	-
f_{13} (Hz)	0.00	0.00	0.01	-
f_{14} (Hz)	0.01	0.03	0.62	-
f_{15} (Hz)	0.01	0.00	0.06	-
f_{16} (Hz)	0.01	0.08	2.11	-